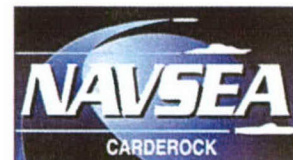# Carderock Division
Naval Surface Warfare Center
West Bethesda, Maryland 20817-5700

NSWCCD-50-TR-2004 / 060   December 2004

Hydromechanics Department
Research and Development Report

Experiment to Examine the Effect of Scale on a Breaking Bow Wave

by

Anna Karion
Thomas C. Fu
Tricia Waniewski Sur
James R. Rice
Don C. Walker
Deborah A. Furey

ISO 9001
Certificate Number 31425

REPORT DOCUMENTATION PAGE

Form Approved
OMB No. 0704-0188

1. AGENCY USE ONLY (Leave blank)	2. REPORT DATE December 2004	3. REPORT TYPE AND DATES COVERED Final

4. TITLE AND SUBTITLE

Experiment to Examine the Effect of Scale on a Breaking Bow Wave

5. FUNDING NUMBERS

6. AUTHOR(S)

Anna Karion, Thomas C. Fu, Tricia Waniewski Sur, James R. Rice, Don C. Walker, Deborah A. Furey

7. PERFORMING ORGANIZATION NAME(S) AND ADDRESS(ES)

Carderock Division, Naval Surface Warfare Center
Code 5600
9500 MacArthur Boulevard
West Bethesda, Maryland 20817-5700

8. PERFORMING ORGANIZATION REPORT NUMBER

NSWCCD-50-TR-2004 / 060

9. SPONSORING / MONITORING AGENCY NAME(S) AND ADDRESS(ES)

Dr. L. Patrick Purtell
Office of Naval Research
800 North Quincy Street
Arlington, VA 22217-5660

10. SPONSORING / MONITORING AGENCY REPORT NUMBER

11. SUPPLEMENTARY NOTES

12a. DISTRIBUTION / AVAILABILITY STATEMENT

Approved for public release; distribution unlimited.

12b. DISTRIBUTION CODE

13. ABSTRACT *(Maximum 200 words)*

A prismatic wedge was towed in fresh water in the David Taylor Model Basin at the Naval Surface Warfare Center, Carderock Division (NSWCCD), generating a large bow wave. Towing speeds ranged from 0.7 to 4.6 m/s, and drafts ranged from 0.6 to 1.5 m. These conditions correspond to Froude numbers from 0.2 to 1.4, Reynolds numbers from 4.1×10^5 to 7.0×10^6 (both based on draft, D) and Weber numbers from 11 to 2800 (based on bow radius, R). In addition to the variations in draft and speed, two different bow geometries were investigated: one with a 20 degree bow entrance angle, 20 degree flare, and sharp leading edge, and one with a 40 degree bow entrance angle, no flare, and rounded leading edge. Measurements of free-surface elevations near the bow were made using a laser imaging technique. High-speed video of the spray generated by the bow wave was also analyzed to yield droplet size and velocity distributions. These measurements provide a useful data set to researchers wishing to validate advanced numerical techniques. Presently, the results are used to investigate scaling issues associated with breaking bow waves.

14. SUBJECT TERMS

Bow wave, breaking wave, spray generation, ship waves

15. NUMBER OF PAGES
47+iv

16. PRICE CODE

17. SECURITY CLASSIFICATION OF REPORT Unclassified	18. SECURITY CLASSIFICATION OF THIS PAGE Unclassified	19. SECURITY CLASSIFICATION OF ABSTRACT Unclassified	20. LIMITATION OF ABSTRACT Unclassified

NSN 7540-01-280-5500

Standard Form 298 (Rev. 2-89)

Contents

This page left intentionally blank.

Figures

This page left intentionally blank.

Tables

This page left intentionally blank.

Abstract

A prismatic wedge was towed in fresh water in the David Taylor Model Basin at the Naval Surface Warfare Center, Carderock Division (NSWCCD), generating a large bow wave. Towing speeds ranged from 0.7 to 4.6 m/s, and drafts ranged from 0.6 to 1.5 m. These conditions correspond to Froude numbers from 0.2 to 1.4, Reynolds numbers from 4.1×10^5 to 7.0×10^6 (both based on draft, D) and Weber numbers from 11 to 2800 (based on bow radius, R). In addition to the variations in draft and speed, two different bow geometries were investigated: one with a 20 degree bow entrance angle, 20 degree flare, and sharp leading edge, and one with a 40 degree bow entrance angle, no flare, and rounded leading edge. Measurements of free-surface elevations near the bow were made using a laser imaging technique. High-speed video of the spray generated by the bow wave was also analyzed to yield droplet size and velocity distributions. These measurements provide a useful data set to researchers wishing to validate advanced numerical techniques. Presently, the results are used to investigate scaling issues associated with breaking bow waves.

Administrative Information

Acknowledgements

Introduction

Bow wave dynamics have been a subject of much theoretical and analytical research in the past (including Ogilvie 1972, Noblesse *et al.* 1991, Fontaine and Cointe 1997, and others). Numerical methods have also been used to investigate free-surface flows near ships (Miyata and Inui 1984, Wyatt 2000, Sussman and Dommermuth 2001, Iafrati and Campana 2003, and others). At present, a large variety of computational methods exists for modeling these flows. As numerical methods have grown more sophisticated, they have begun to attempt to model the breaking bow wave. Experimental data in this

1

breaking region are needed for validation of these advanced numerical techniques. While previous experiments have also investigated bow waves (Ogilvie 1972, Dong *et al.* 1997, Miyata and Inui 1984, Waniewski *et al.* 2002, Roth *et al.* 1999), most were conducted at lower Reynolds numbers and did not exhibit energetic breaking. Turbulence and velocity measurements in two-dimensional breaking ocean waves were conducted by Melville, *et al.* (2002) on a larger scale. Surface roughness measurements, similar to those presented here, were presented by Walker, *et al.* (1996) for a two-dimensional steady breaking wave. The experiment described in this paper was designed to generate a large three-dimensional bow wave with energetic breaking and substantial bubble and spray generation.

The present experiment provides data on free-surface elevations near the bow of a simple wedge. The simple hull geometry of the model renders the data especially useful for the validation of numerical computations. The towed model was also exceptionally large, generating a large amplitude bow wave. The measurements thus provide a good test for evaluating the importance of nonlinear effects in numerical predictions. Measurements of spray droplet size and velocity distributions can also be used to validate advanced numerical techniques that account for spray. Results from this experiment can also be found in Karion, *et al.* (2003).

The experiments were conducted in fresh water at a variety of speeds and drafts, and thus a variety of Froude, Reynolds, and Weber numbers. The resulting data set is used to study how the bow wave characteristics, such as free-surface height and spray generation, vary with these parameters. In addition to investigating the effect of Froude and Reynolds numbers, the present experiment also investigates the effect of bow geometry. Two different bow geometries and leading edges are used to generate bow waves under otherwise identical conditions. The differences in the shape, height, and spray characteristics of the resulting bow waves can help researchers begin to understand the influence of bow shape on breaking.

Experimental Description

A large bow wedge model (Model No. 5605) was towed in the Deep Water Towing Basin (Carriage 2) at the David Taylor Model Basin of the Naval Surface Warfare Center, Carderock Division. The tow basin under Carriage 2 is 15.5 m wide and approximately 575 m long. It is usually filled with fresh water to a depth of 6.7 m, but for this experiment the water level was lowered to 6.3 m to accommodate the large model at the 1.52 m draft. It was lowered accordingly for the lower drafts, as the model itself remained at a constant height above the basin floor. A plan view of the Carriage 2 facility is included in Figure 1.

Model No. 5605 is a large prismatic wedge with dimensions as indicated in Figure 2. One end (referred to as the fine bow) has a 20 degree entrance angle and is flared at 20 degrees, with a fine leading edge (0.16 cm radius of curvature). The other end (referred to as the full bow) has a 40 degree entrance angle and is straight-sided, with a rounded leading edge (1.27 cm radius of curvature). For the first part of the experiment, the model was towed with the fine bow forward, and for the second part, the model was
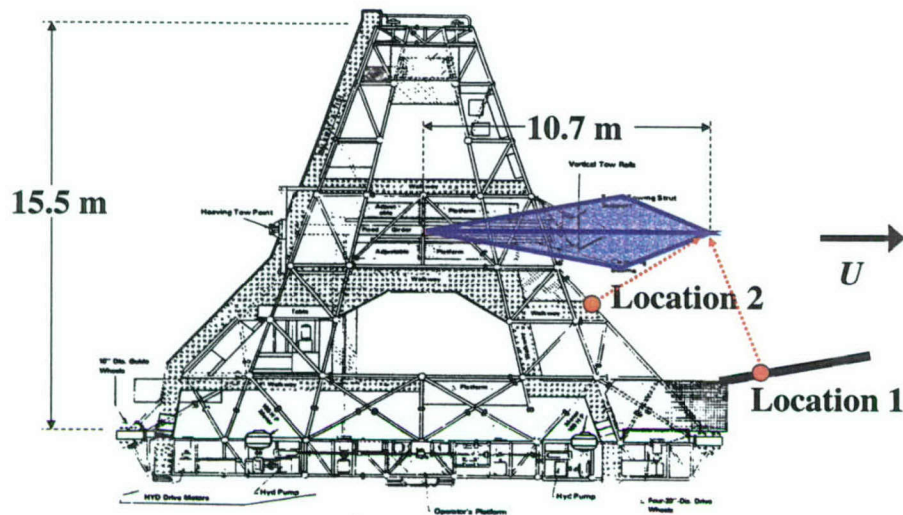
Figure 1. Schematic diagram of the 10.7 m long bow wedge model (blue diamond) and the 15.5 m wide towing carriage, viewed from above. The two locations used for the high-speed video camera are indicated by the red circles, and the camera look directions are indicated by the red arrows.
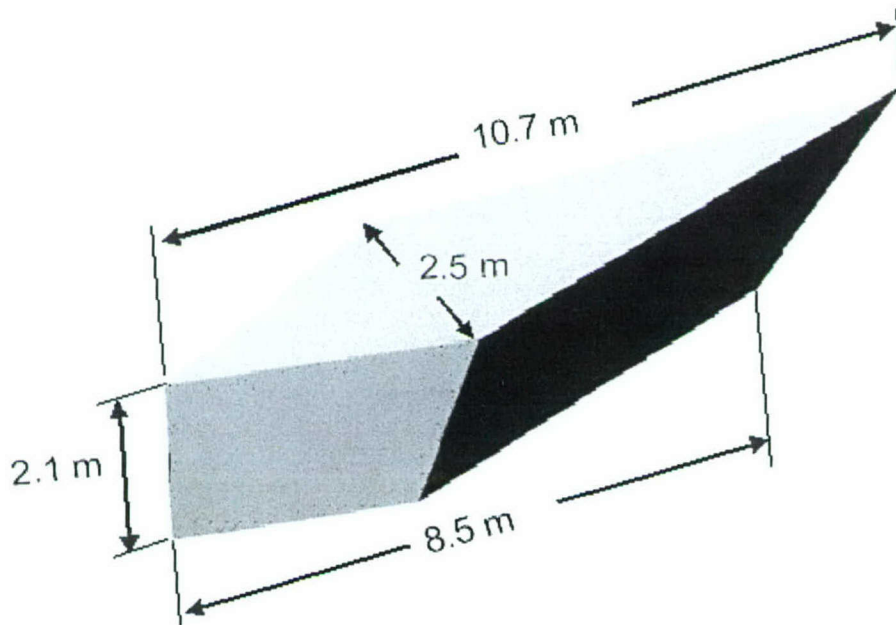
Figure 2. Diagram of wedge model with dimensions (in meters). The fine bow is on the right in the figure, and the full bow on the left.

3
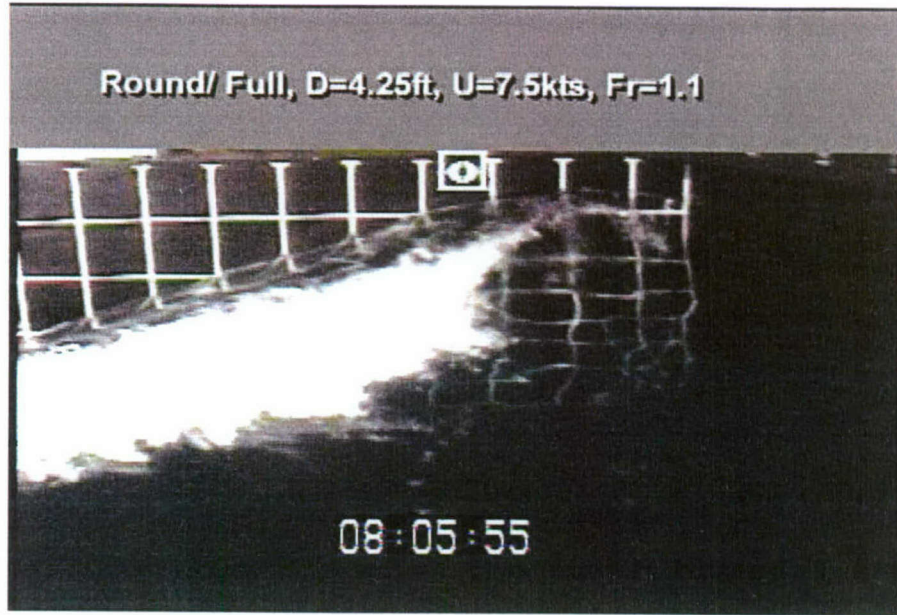
Figure 3. Example of the bow wave generated by the full bow at $D = 1.3$ m and $U = 3.9$ m/s. The model is painted black with a white grid. The vertical grid spacing is 30.5 cm, and the horizontal spacing is 30.5 cm if measured along the centerline of the model. The small horizontal marks at the top of the grid are the top of the model.

mounted in the opposite direction (with the full bow forward). Thus, measurements of the free-surface and the spray were made for both configurations. Figure 3 shows an example of the bow wave generated by the full bow (in the photograph, the model is running from left to right).

The run conditions are summarized in Table 1 for the fine bow and Table 2 for the full bow. In the tables, D represents the draft (the immersion depth of the model, measured from the free-surface at zero velocity), U the towing velocity, and Fr, Re and We the Froude, Reynolds and Weber numbers respectively. The numbers are defined as follows:

$$Fr = \frac{U}{\sqrt{gD}} \tag{1}$$

$$Re = \frac{UD}{\nu}, \tag{2}$$

$$We = \frac{\rho U^2 R}{\sigma}, \tag{3}$$

where g is the coefficient of gravitational acceleration, R is the bow radius, ν is the kinematic viscosity of fresh water, ρ is the density of fresh water, and σ is the surface

4

Table 1. Matrix of run conditions for the fine bow.

D (m)	U (m/s)	Fr	Re ($\times 10^{-6}$)	We ($\times 10^{-2}$)	QViz data	Spray
0.61	0.7	0.3	0.4	0.11	Yes	No
0.61	1.4	0.6	0.9	0.43	No	No
0.61	2.0	0.8	1.2	0.87	Yes	No
0.61	2.9	1.2	1.8	1.8	Yes	Yes
0.61	3.9	1.6	2.3	3.3	No	Yes
1.07	0.9	0.3	0.9	0.18	Yes	No
1.07	2.6	0.8	2.7	1.5	Yes	Yes
1.07	3.9	1.2	4.1	3.3	Yes	Yes
1.07	4.6	1.4	4.9	4.6	No	Yes
1.52	0.7	0.2	1.0	0.11	Yes	No
1.52	1.0	0.3	1.6	0.22	Yes	No
1.52	2.0	0.5	3.0	0.87	Yes	No
1.52	3.1	0.8	4.7	2.1	Yes	N/A
1.52	3.3	0.9	5.0	2.4	No	Yes
1.52	3.6	0.9	5.5	2.8	No	Yes
1.52	3.9	1.0	5.9	3.3	Yes	Yes
1.52	4.6	1.2	7.0	4.6	Yes	Yes

Table 2. Matrix of run conditions for the full bow.

D (m)	U (m/s)	Fr	Re ($\times 10^{-6}$)	We ($\times 10^{-2}$)	QViz data	Spray
1.07	0.9	0.3	0.9	1.5	No	No
1.07	1.7	0.5	1.8	5.3	Yes	No
1.07	2.6	0.8	2.7	12	Yes	Yes
1.07	3.1	1.0	3.3	18	Yes	Yes
1.30	3.3	0.9	4.3	20	No	Yes
1.30	3.6	1.0	4.6	24	No	Yes
1.30	3.9	1.1	5.0	28	No	Yes
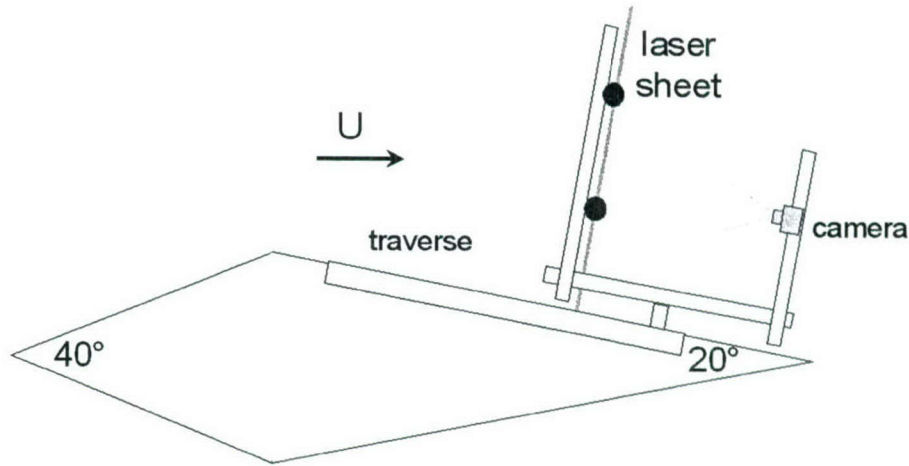
Figure 4. Diagram of laser sheet and camera setup, viewed from above. In this case, the model would be moving from left to right. When the full bow was forward, the traversing system was mounted on the full bow.

tension at a clean air-freshwater interface. The column labeled "QViz data" indicates whether data was acquired using the QViz system (described below). The column in the tables labelled "Spray" indicates whether spray was observed in the bow wave region. High-speed video was taken for all of the conditions for which spray was observed. High-speed video was also taken for many conditions for which spray was not observed, but these images were not processed.

Quantitative Visualization (QViz)

Technique Description

A non-intrusive optical technique, Quantitative Visualization (QViz), has been used to measure the free-surface disturbances occurring in regions commonly inaccessible to more traditional measurement methods, i.e. near wake flows, bow sheets and breaking waves. These regions are generally difficult to quantify due to the multiphase aspect of the flow as well as their very unsteady nature. However, the unsteady surfaces, droplets and bubbles in these regions are effective scatterers and allow for optical imaging of the deformations in the surface. With a laser sheet and digital camera, the QViz system illuminates the surface of interest and collects digital images representing instantaneous cross sections of the spray envelope and surface profiles (Furey and Fu (2002)).

Setup

In the current experiment, a laser light sheet was projected onto the water surface perpendicular to the side of the hull. The light sheet was generated by a diode-pumped,

6

solid-state YAG laser, with an output of 2.5–3.5 W at 532 nm (Model MLM-0532 by Melles-Griot), fed through two fiber optic cables. A standard video camera, mounted facing aft, collected images of the laser sheet reflection off the water surface. The camera and fiber optic laser probes were mounted to a rail system that was attached to a traverse, which was in turn mounted on the model itself (see Figure 4). The two laser fiber optic probes formed a laser sheet approximately one meter wide. The camera was mounted approximately 1.5 meters forward of the laser sheet and angled down towards the water surface. Midway through testing, a second camera was mounted aft of the sheet, facing forward, to capture video of the light sheet from the opposite direction as well (this second camera is not shown in the figure). This camera enabled viewing of the laser sheet in the trough of the wave, which was blocked from the forward camera by the wave crest. The traversing system was automated and coupled with the data acquisition software so that once the desired number of images was acquired, the laser sheet and camera system moved aft together and the camera began acquiring images at a new position. Thus, depending on the run time, many positions were covered on each pass down the basin. Images were collected for 2 seconds at 30 frames per second at each of approximately 180 locations along the hull (every 2.54 cm) for the fine bow, and 115 locations for the full bow.

Digital images from the video camera were collected at 30 frames per second using a National Instruments frame-grabber board and a personal computer. An image analysis program was developed at NSWCCD using National Instruments LabView software with the Image Processing (Vision) toolbox using built-in edge-detection routines to extract the surface profile information. To process the averaged surface contour plots, sequential images (usually 30 images, representing one second of data) were averaged together, effectively providing a time-averaged profile. This averaged image was then analyzed using image filtering and search routines to identify the boundary of the free-surface. The image size was 640×480 pixels, covering a viewing area of approximately 1.5×1.2 meters. Thus the lowest possible uncertainty (approximately 1 pixel) was equal to 0.25 cm. If a particular location was also analyzed using an image from the forward-facing camera that was added later, the wave profiles from the forward and aft-looking cameras were averaged. The resulting wave profiles were interpolated to generate surface contour plots shown in the Results section.

The image processing method for calculating free-surface roughness and fluctuations in the breaking region was slightly different from that described above. For the breaking analysis, the breaking region of each image was analyzed separately, and the resulting water line determined as a function of time.

The images collected in this experiment were taken with an interlaced camera, so that each image was acquired in two fields, 1/60 of a second apart in time. In an interlaced image, the first field is composed of the odd pixel lines and the second the even. For the breaking analysis of each image, these fields were separated to minimize the blurring of the moving surface (the shutter speed of the camera was also at 1/60 second). (This separation was not necessary when the images were averaged to generate the contour maps). The effective vertical resolution for each image was thus halved to

7
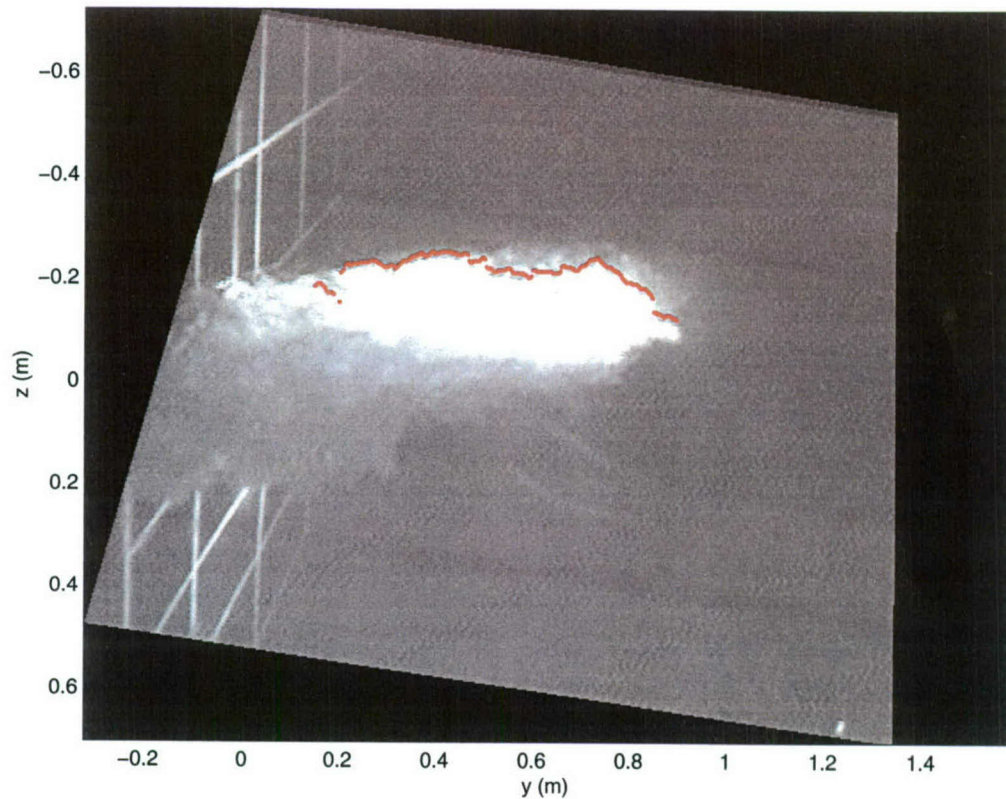
Figure 5. Example of a QViz image of the bow wave generated by the full bow, with the edge detected by the data analysis algorithm superimposed in red. The speed of this run is 2.6 m/s, and the draft is 1.1 m.

240 pixels, and the number of images doubled. The LabView software used to perform this separation of the interlaced fields simply interpolated to regenerate the intermediate pixels. Thus, at each location, the two seconds of data at 30 frames per second, each composed of two fields, resulted in 120 images for analysis.

An example of an image that has been analyzed in this way is shown in Figure 5. The red line superimposed on the surface of the wave is the edge that has been extracted using the analysis. The sides of the image seem distorted because the image has been processed using a calibration grid to correct for the distortion due to camera placement. The model appears on the left side of the image.

Calibration

Distortion due to camera placement and viewing angle was corrected using an image of a calibration grid with equally spaced points and a calibration algorithm in National Instruments' LabView IMAQ Vision software package. The largest error in the system

8

was introduced by the camera placement and the calibration method. For example, error in the calibration would result if the grid was not held perfectly square and at the correct distance relative to the camera. It is estimated that the total error on the free-surface elevations is ±1cm. However, this is an error affecting the determination of the absolute location of the free surface. The relative error in the free-surface measurement from one frame to the next (affecting the fluctuations of the surface) is much lower, estimated to be at the pixel error value of 0.25 cm. Future effort to reduce the error on these types of measurements is focusing on placing the cameras on automated pan-and-tilt units, so that their orientation is exactly known, and the calibrations can be performed in a more controlled environment.

High-speed imaging of spray droplets

A digital high-speed video camera (Photron FASTCAM-PCI 2K) was used to investigate the spray produced by the breaking bow waves. The imaging sensor of this camera is a square pixel, progressive scan CCD (Charge-Coupled Device). The scan area is 4.8 (H) x 3.6 (V) mm or 1/3 inch format. The resulting images are eight-bit monochrome or grayscale. The high-speed video camera head is 5 (W) x 5 (H) x 11.5 (D) cm. The memory of the PCI-compatible control card is 512 MB, which allows the camera to record and store 2,176 full resolution frames per image series. Various camera parameters may be set using the FASTCAM-PCI control software. For example, the frame rate is adjustable from 30 to 2,000 frames per second. Full resolution (512 x 480 pixels) images can be achieved up to 250 frames per second. Additional technical specifications for the high-speed video camera are available on the manufacturer's internet website, http://www.photron.com. For these experiments, the frame rate was set at 250 frames per second and a shutter speed of at least 1/500 second was used. A C-mount motorized zoom lens (Computar M6Z1212M) was used with the high-speed camera. The lens contained three motors for the aperture, focus, and zoom that could be controlled remotely.

Two different locations were used for mounting the high-speed video camera head (see Figure 1). Location 1 was on a boom which extended from the carriage, roughly parallel with the starboard side of the model and Location 2 was on the edge of a carriage catwalk. These locations were chosen so that the spray droplets would appear light in color against a dark background in the images. In Location 1 the bow wedge model provided a dark background, and in Location 2 the undisturbed free surface was used as the background. In addition, Location 1 provided a view of the bow spray similar to field observations of bow spray on the R/V Revelle in March 2001 (also funded by the Office of Naval Research). After the experiments, it was found that detailed analysis of the spray droplet characteristics was possible with the images taken from Location 2 but not from Location 1. There were two principal reasons that the images from Location 1 were not suitable for analysis. First, the boom used in Location 1 was subject to vibrations which contaminated droplet velocity measurements. Second, it was observed that the bow spray was not thrown upwards as dramatically as it was in the field. The spray droplets tended to fall vertically down immediately after their

9

creation with the breaking wave in the background, so there was not enough contrast to resolve individual droplets.

The camera was mounted on a remote controlled positioning unit capable of horizontal (pan) and vertical (tilt) motion (Pelco PT280-24SL). A cable connected the pan/tilt positioning unit to the pan/tilt and lens control unit (Pelco PT506-24DT). The control unit uses an eight-position joystick to control pan/tilt movements, and the lens functions and speed are controlled by three momentary paddle switches and a rotary knob. The control unit did not have position readouts; therefore, the tilt angle was measured with a inclinometer accurate to 0.1 minutes after each tilt angle adjustment.

Prior to the experiments, images of a grid distortion target (Edmund Industrial Optics, PN: 46249, NIST traceable certification of accuracy SN: 000-0097) were taken to measure the depth of field and to verify the number of pixels per mm for the working distances used in these experiments. The images of the spray created in these experiments were processed using algorithms written in MATLAB with the Signal and Image Processing toolboxes. These algorithms extract quantitative characteristics of the spray droplets such as size and velocity distributions. A detailed description is given in Fu *et al.* (2003). The greatest source of error in this technique arises from the depth of field uncertainty. For example, at a working distance of 3.9 m, a 2.3 mm radius droplet could appear as 2.7 mm radius droplet if it was at the near edge of the depth of field and appear as a 2.0 mm radius droplet if it was at the far edge of the depth of field.

Results

This section presents the results from both the QViz and high-speed video measurement systems.

Contour Plots of Free Surface

QViz data was used to generate contour plots of the free surface of the bow wave for both the fine and full bows. In all of the contour plots shown, the horizontal (x) axis represents the distance along the model centerline, with the origin at the intersection of the water line with the bow. The vertical (y) axis represents the lateral distance from the centerline of the model. The elevations represented by the various colors are shown in the colormap key on the right of each figure. Figures 6, 7, and 8 compare free-surface contours for the fine bow at the same Froude number but three different Reynolds numbers (both the draft and speed were varied). Contours for a Froude number of 0.8 at Reynolds numbers of 1.2×10^6, 2.7×10^6, and 4.7×10^6 are shown in these figures. Figure 9 shows the free-surface contour of the bow wave generated by the full bow at the same Froude number and Reynolds number of 2.7×10^6. The solid black line in the figures represents the location of the model. As was mentioned in the previous section, often the trough behind the first bow wave was shadowed by its crest. Therefore, in some cases, the contour plots are incomplete. The blank regions indicate areas where there was not enough good data to extract the surface information.

Figures 6, 7, and 8 illustrate that the free-surface elevation of the crest increases with the Reynolds number of the flow, although the qualitative shape of the wave remains
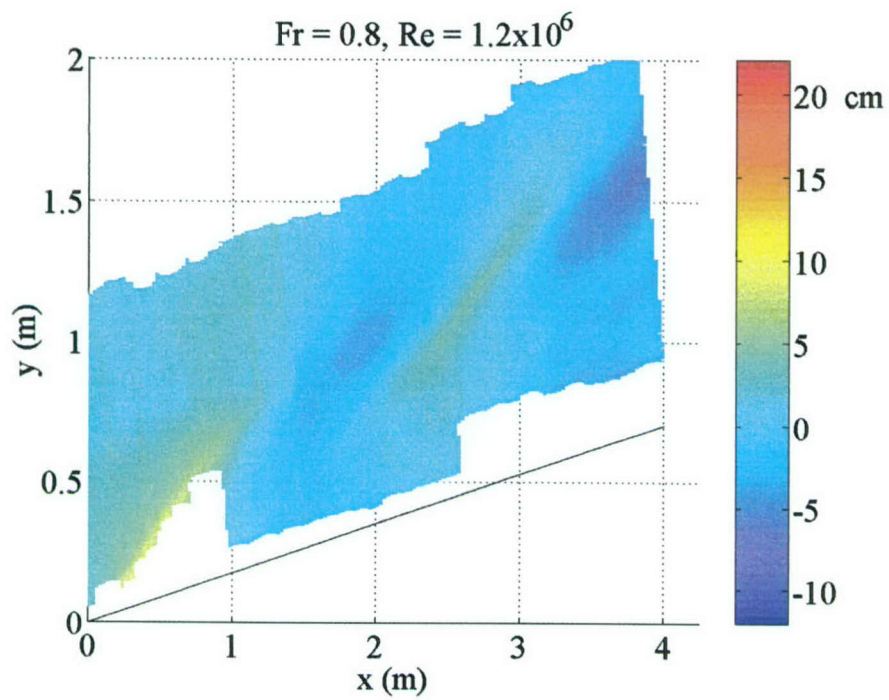
Figure 6. Free-surface elevations for fine bow at $Fr = 0.8$ and $Re = 1.2 \times 10^6$.
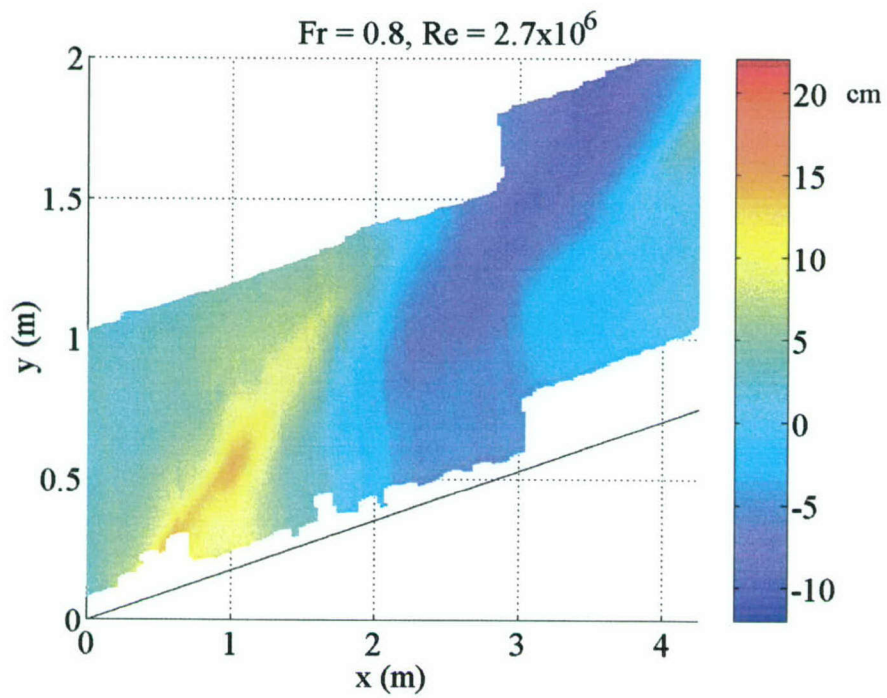
Figure 7. Free-surface elevations for fine bow at $Fr = 0.8$ and $Re = 2.7 \times 10^6$.

11
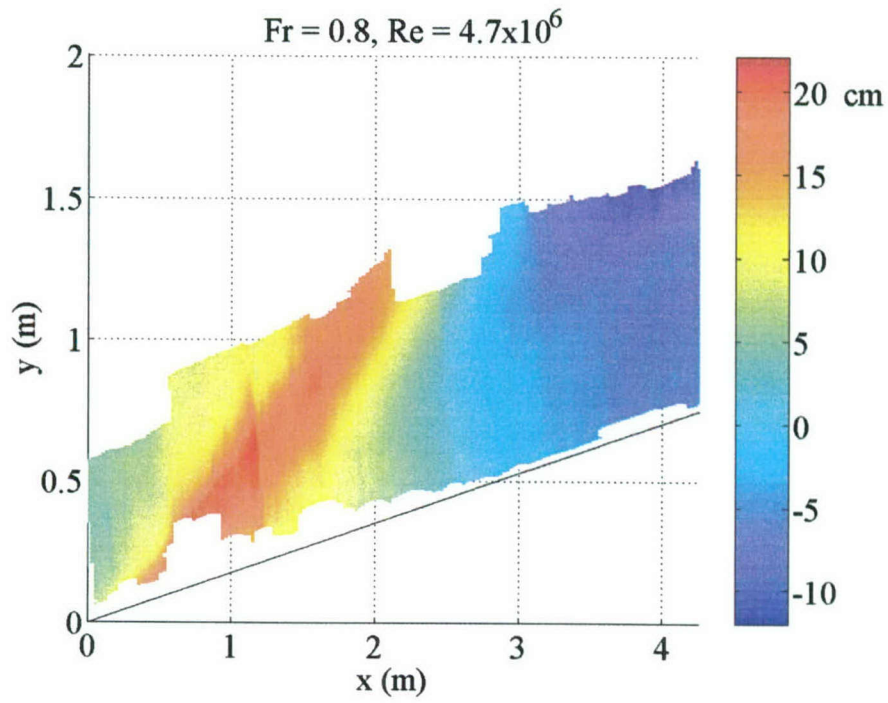
Figure 8. Free-surface elevations for fine bow at $Fr = 0.8$ and $Re = 4.7 \times 10^6$.
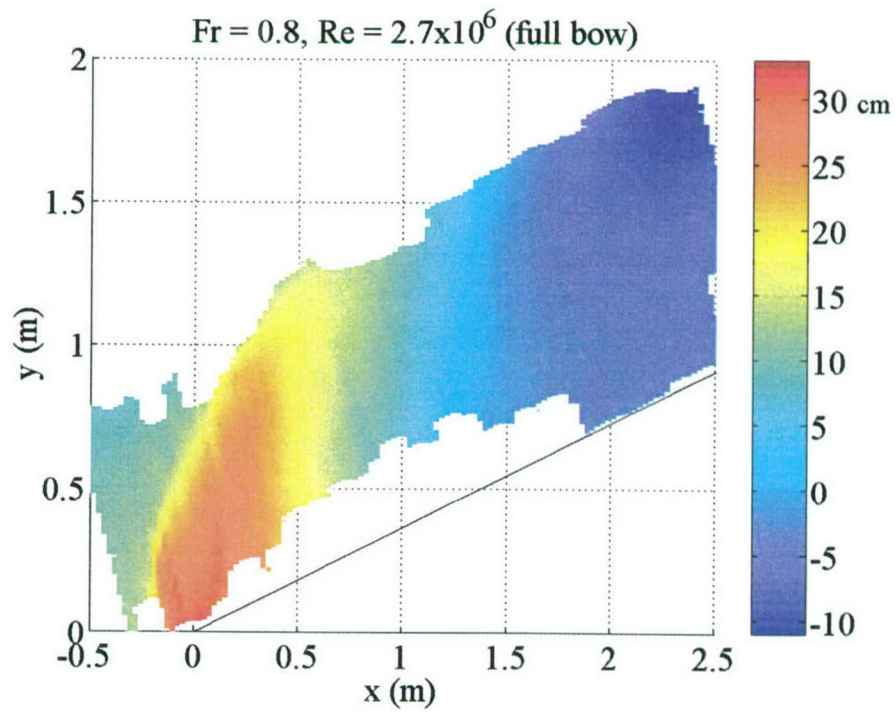
Figure 9. Free-surface elevations for full bow at $Fr = 0.8$ and $Re = 2.7 \times 10^6$.
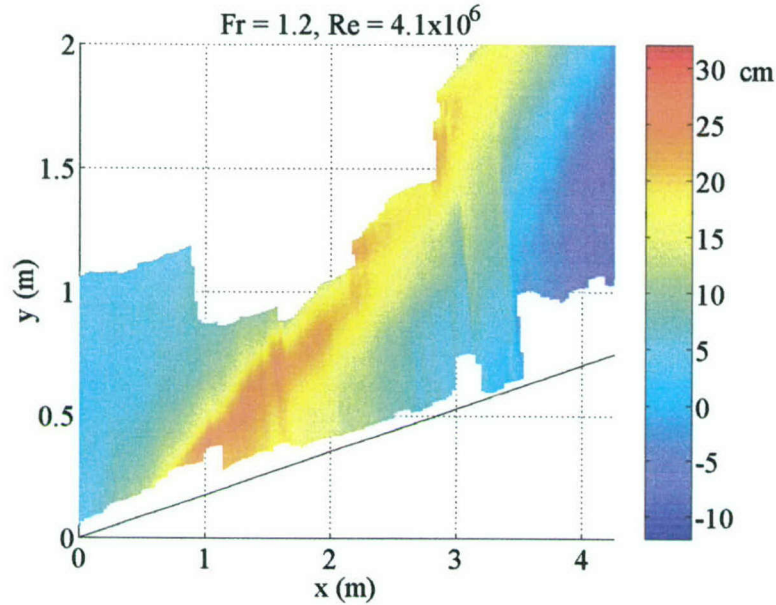
Figure 10. Free-surface elevations for fine bow at $Fr = 1.2$ and $Re = 4.1 \times 10^6$. The velocity is 3.9 m/s, and the draft is 1.07 m.

similar. A comparison of Figures 7 and 9, which show the free-surface elevations for the same conditions but for the two different bow shapes, indicates that the hull shape has a substantial effect on the bow wave. It should be noted that the color scale on the two figures differs. The wave generated by the full bow is larger in amplitude, and the crest occurs closer to the hull and farther forward than for the fine bow. These characteristics were also observed visually during the test. The two bows were different in three ways: the flare angle, the entrance angle, and the roundedness of the leading edge. Further testing of each of these independent factors is necessary to determine how each affects the wave shape.

Ship draft has previously been shown to be the dominant length scale in bow wave dynamics (Ogilvie 1972, Miyata and Inui 1984, Waniewski et al. 2002); in this experiment the draft was varied to observe its effect on the bow wave characteristics. Figures 10 and 11 show the free-surface contours for two runs with the fine bow at the same speed of 3.9 m/s but two different drafts. Figure 10 shows the contours at a draft of 1.07 meters ($Fr = 1.2$), while Figure 11 shows the contours at a draft of 1.52 meters ($Fr = 1.0$). A comparison of the two figures shows that the draft of the model does affect the wave height, although it does not appear to affect the general wave shape and form. The maximum wave height at the 1.07 m draft is 25 cm, while at 1.52 m it is 30 cm.

Figure 12 shows the contours for $Fr = 0.5$ and $Re = 3.0 \times 10^6$ for the fine bow. This elevation contour plot can be contrasted with that at a slightly lower Reynolds

13
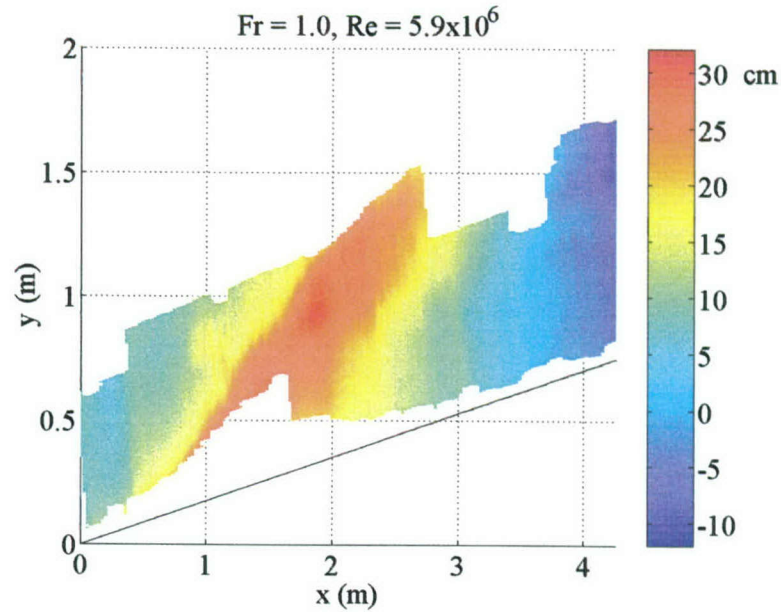
Figure 11. Free-surface elevations for fine bow at $Fr = 1.0$ and $Re = 5.9\times10^6$. The velocity is 3.9 m/s, and the draft is 1.52 m.

number (2.7×10^6) but a larger Froude number of 0.8, shown in Figure 7. Comparison of these two figures shows that the height of the bow wave formed at the higher Froude number is larger, despite having a Reynolds number that is approximately 10% lower. The scaling of the maximum wave height with the various flow parameters varied in this experiment will be discussed in the following section.

A key goal of this experiment is to provide useful data for comparison with various numerical models. As an example, the experimental data for the fine bow experiment at $Fr = 1.2$ and $Re = 1.8 \times 10^6$ is compared in Figure 13 with prediction results from Das Boot, a computational program developed at SAIC by D. Wyatt. Das Boot is a fully non-linear free-surface potential-flow code (for more information on Das Boot, see Wyatt (2000)). The free-surface elevation contours on the top half of the figure are from the experimental data; the contours on the lower half of the figure are from the numerical simulation. The black filled triangle in the center represents the location of the model. The simulation compares quite well with the experiment, although the wave heights appear to be slightly underpredicted.

Surface Fluctuations

The Quantitative Visualization (QViz) data was used to determine the variation of the free surface with time. Two seconds of data images were collected at each fixed laser sheet location; these were analyzed to determine the fluctuation of the free surface. Surface fluctuations were determined only on the breaking region of the bow wave; that

14
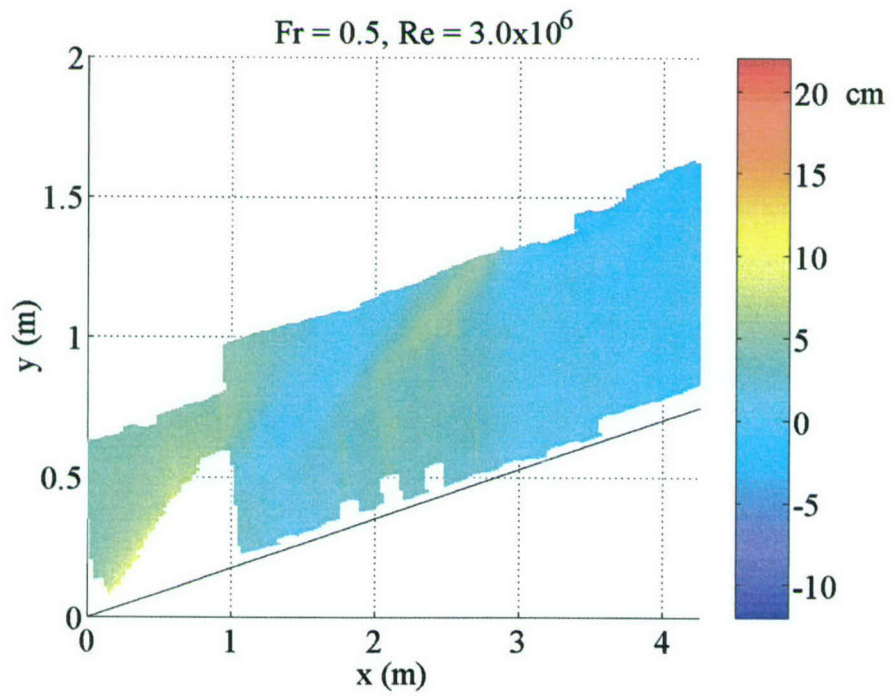
Figure 12. Free-surface elevations for fine bow at $Fr = 0.5$ and $Re = 3.0 \times 10^6$. The velocity is 2.0 m/s, and the draft is 1.52 m.
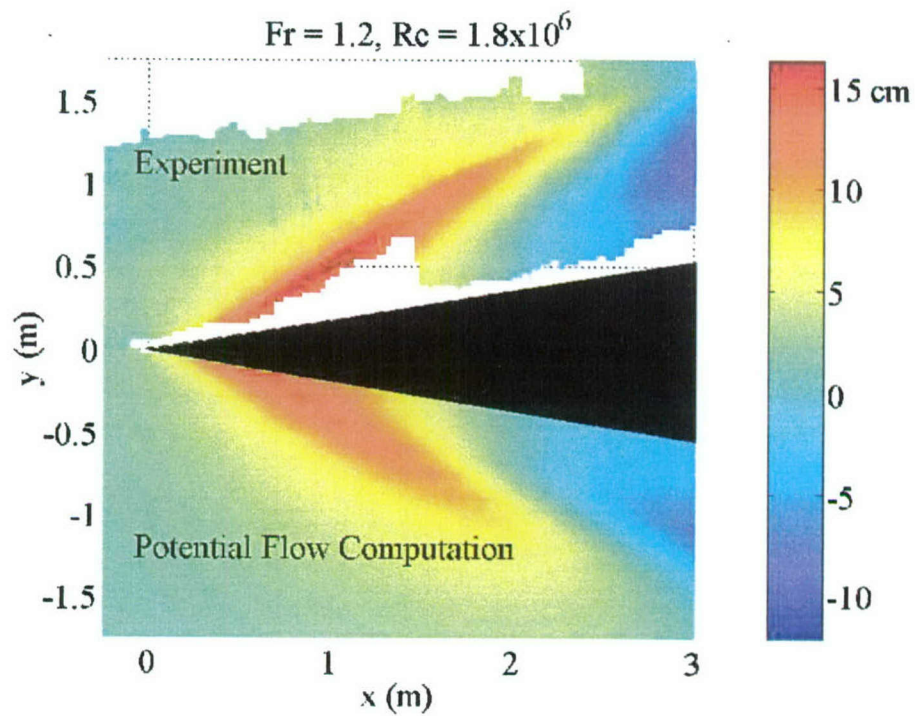
Figure 13. Comparison of data with computational prediction (courtesy of Don Wyatt) for $Fr = 1.2$, $Re = 1.8 \times 10^6$.

Fine Bow Wave Profile, D = 1.5 m, Fr$_{\text{D}}$ = 1.0, U = 3.9 m/s (7.5 kt), X = −2.6 m
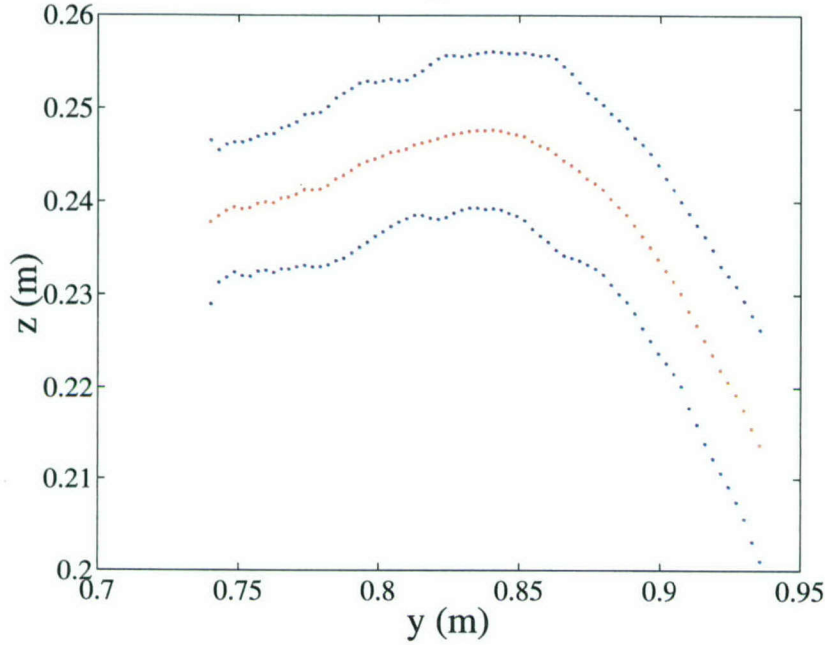
Figure 14. An example of the mean free-surface location in the breaking region, in the red points, with the blue dots showing the band one standard deviation away. The standard deviation is calculated for each point based on an analysis of 120 frames over two seconds.

is, in the region beginning where the bow sheet first impinged back onto the free surface. In this area, the laser light sheet was scattered very effectively due to the turbulent, multiphase nature of the flow. Therefore, the region analyzed was that where the image was clearly and significantly brighter than the surrounding background. The image was thresholded at a high pixel value that differed based on the condition, but was usually at an approximate value of 200 out of 255, and then the edge-detection algorithm was executed to find the top-most edge. Because this region had high contrast levels, the image processing revealed relatively accurate measurements of the free surface. The non-breaking parts of the free surface, although previously analyzed in a mean fashion for the contour plots, were not clear enough for a frame-by-frame analysis.

The free-surface location was determined for each of the 120 images at a certain laser sheet position, and its mean calculated as a function of y position along the wave, where y is defined as the distance from the model's centerline, in the direction perpendicular to the hull (i.e., along the laser sheet). The standard deviation of this mean was also calculated as a function of location in the sheet, y. An example of the result is shown in Figure 14 for the fine bow at $Fr = 1.0$. The band around the mean
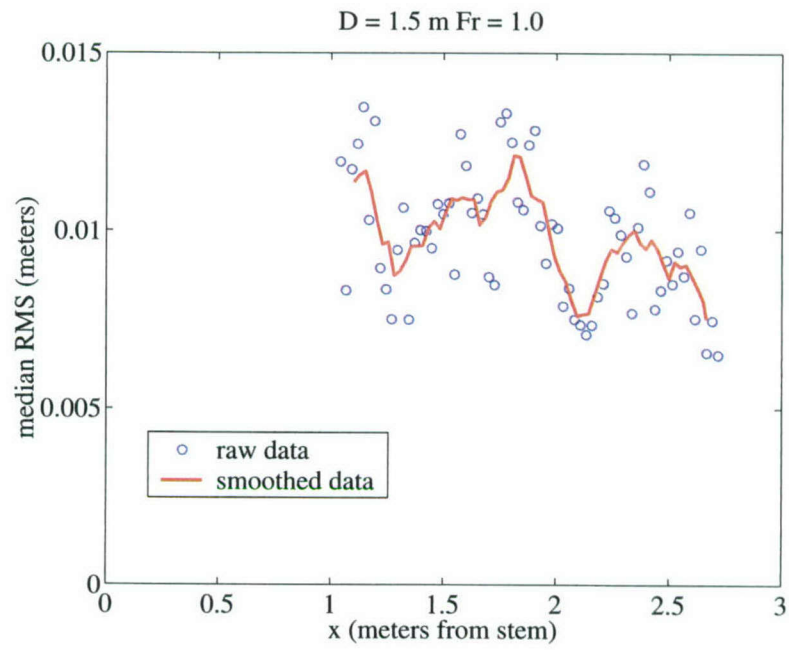
Figure 15. Standard deviation of the free-surface profile as a function of distance along the hull, x, for the fine bow at $Fr = 1.0$, $D = 1.5$ m, and $U = 3.9$ m/s.
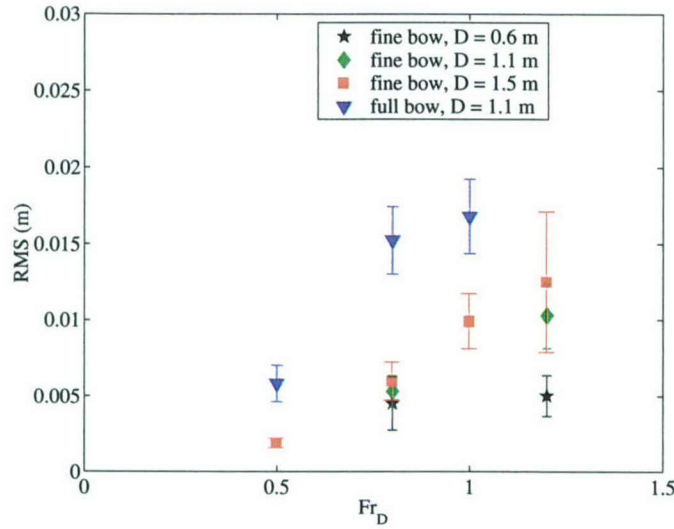
Figure 16. Median standard deviation of the free-surface profile, as a function of draft Froude number. The error bars represent the standard deviation for each point.

free-surface profile indicates the magnitude of the fluctuations at each location along the free-surface profile.

The median of the standard deviation along the y dimension is shown as a function of x, the distance along the hull, for the fine bow at $D = 1.5$ m and $Fr = 1.0$ in Figure 15. The magnitude of the fluctuations varies significantly along the hull with no apparent trend, for this and the other conditions. It was observed, when analyzing the fluctuations from one run to another and correlating them to the time of day of the run, that the fluctuation magnitude was significantly lower for runs performed when the basin water was its calmest (for example, for the first run of the day or after a long break). The results show that fluctuations in the free surface of the wave are strongly dependent on the initial conditions. During the experiment, these initial conditions were not tightly controlled. Although the wait time between runs was roughly constant at 30 minutes, some runs were performed when the water was significantly calmer, such as the first run of the day or after a long break in runs to make an equipment repair. There was also an effort made not to run a fast speed immediately following a slower-speed run, but this was not always possible due to tight scheduling.

Figure 16 shows the median value of the standard deviation (taken over all positions x) as a function of draft Froude number. There is considerable scatter in the data, due to the reasons explained above. Figure 17 shows the same data normalized by the maximum average wave height for each condition. This figure shows that in general, the magnitude of the surface fluctuations scales with the maximum wave height, and varies from between two and six percent.

19
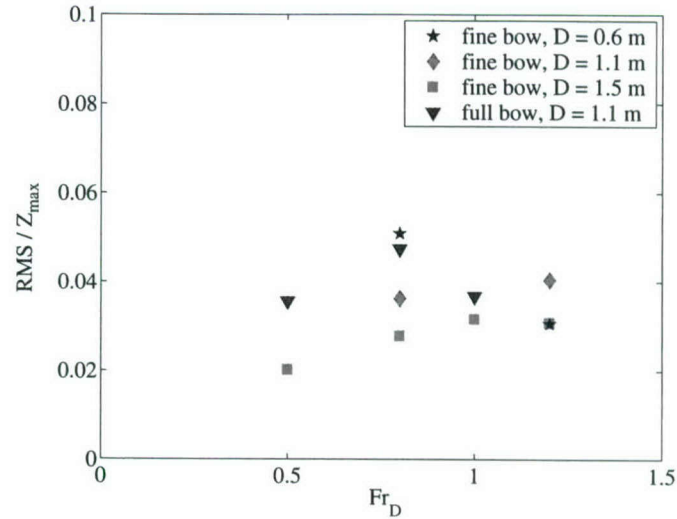
Figure 17. Median standard deviation of the free-surface profile, normalized by the maximum wave height, as a function of draft Froude number. The standard deviation for each point ranges from 0.005 to 0.02.

Surface Roughness Measurements

Wavenumber spectra have been constructed by performing a fast-fourier transform of each detected edge (i.e. the free-surface profile for each frame). The goal of performing these transforms was to establish a spectrum of the turbulent length scales in the breaking region of the wave, and to determine whether the spectrum changes with the wave conditions, such as Froude number. Spectra were only calculated for the full bow because the surface of the breaking region of the fine bow was too short in length, usually ten centimeters or less. The straight-sided bow with its rounded leading edge produced a wide breaking wave, as contrasted with the narrow, plunging breaker of the fine bow. The reflection of the laser sheet off of the wide breaking region of the wave provided a free-surface profile that was long enough to allow for performing the FFT (see Figure 5).

The resulting wavenumber spectra are shown in Figure 18 for two different speeds (2.6 m/s and 3.1 m/s) at two different locations (0.5 m and 0.75 m from the stem). The location does not seem to have an effect on the spectrum. The spectrum for each speed, averaged over the 25 locations for which there was sufficient data, is shown in Figure 19. The locations used were the range from 0.38 m to 1.02 m aft of the stem. The draft is 1.1 meters. The wavenumber results show that the power spectrum at the higher wavenumbers, or shorter wavelengths (under approximately 3 cm), does not vary significantly with Froude number. This result is consistent with results shown for a two-dimensional spilling breaker by Walker, *et al.* (1996). It appears that the breaking

20
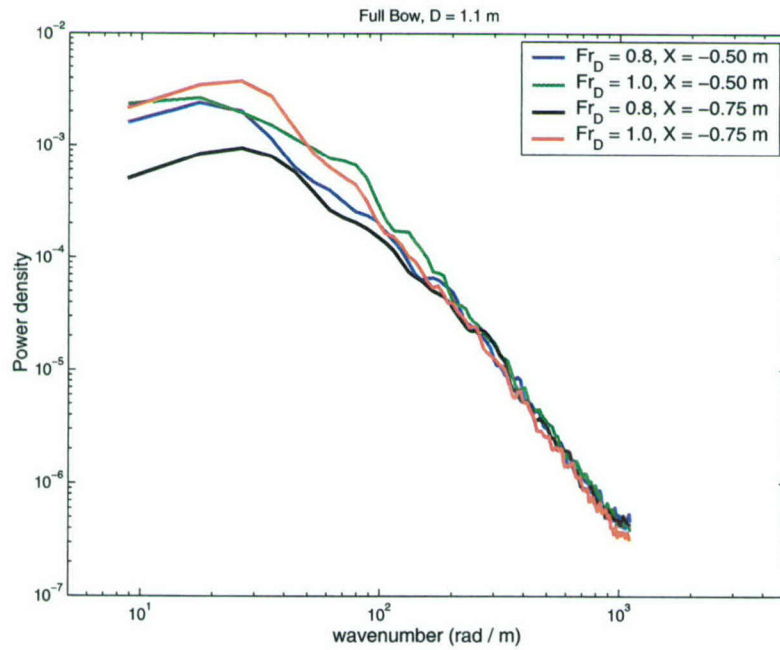
Figure 18. Wavenumber spectrum for the breaking region of the bow wave for the full bow at two velocities (2.6 m/s, or Fr = 0.8, and 3.1 m/s, or Fr = 1.0) and at two locations along the hull.
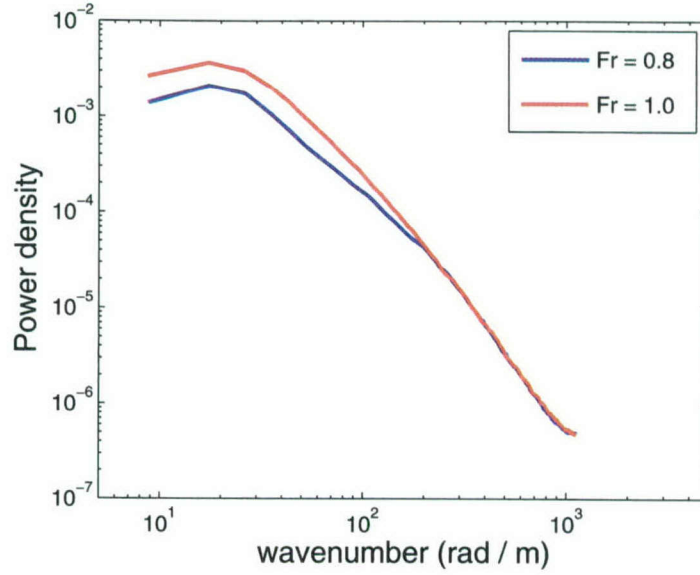
Figure 19. Average wavenumber spectrum over 25 locations (covering 0.6 m) for the breaking region of the bow wave for the full bow at two velocities (2.6 m/s, or Fr = 0.8, and 3.1 m/s, or Fr = 1.0).

at the higher speed (Fr = 1.0) have slightly more energy at lower wavenumbers than the two cases at lower speeds. However, this phenomenon would need to be studied experimentally in more detail in the future to make a firm conclusion. These somewhat limited results do support the conclusions of Walker, *et al.* (1996), however.

Extent of Breaking

The extent of breaking occuring in the bow wave for each condition was determined from the QViz images. Essentially, for each image, the region in which the laser reflected very brightly off of the surface was defined as the breaking area. This was the area in which the laser reflected off of the multiple air-water interfaces of the wave. Although this determination is somewhat subjective, it was found that there was a very clear contrast in the images between this region and the rest of the free surface, and effort was made to be consistent. This was the same region that was used for the surface fluctuation and surface roughness analyses described above.

Figures 20 and 21 show contour plots of the free surface with the breaking area, as defined above, superimposed in black, for the fine bow and full bow, respectively. It should be noted here that the contour plots are the same as those in Figures 11 and 9 earlier in this section.

The mean width of the breaking region in the direction perpendicular to the hull (i.e., in the plane of the laser sheet) for the fine bow is shown in Figure 22 as a function
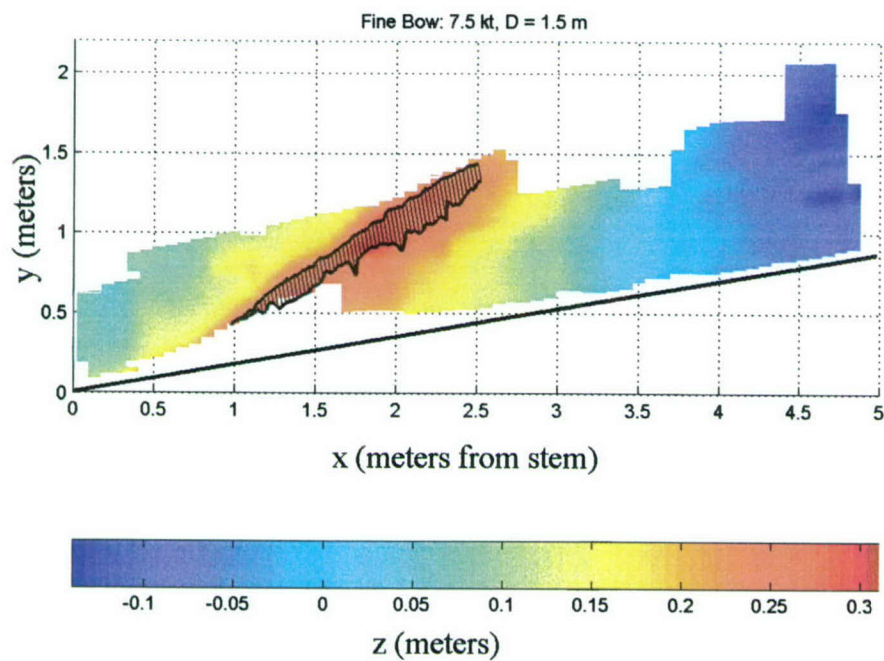
Figure 20. Contour plot of free-surface height with the location of breaking superimposed in black. This run is for the fine bow, and has $D = 1.5$ m, $U = 3.9$ m/s (7.5 kt) and $Fr = 1.0$.
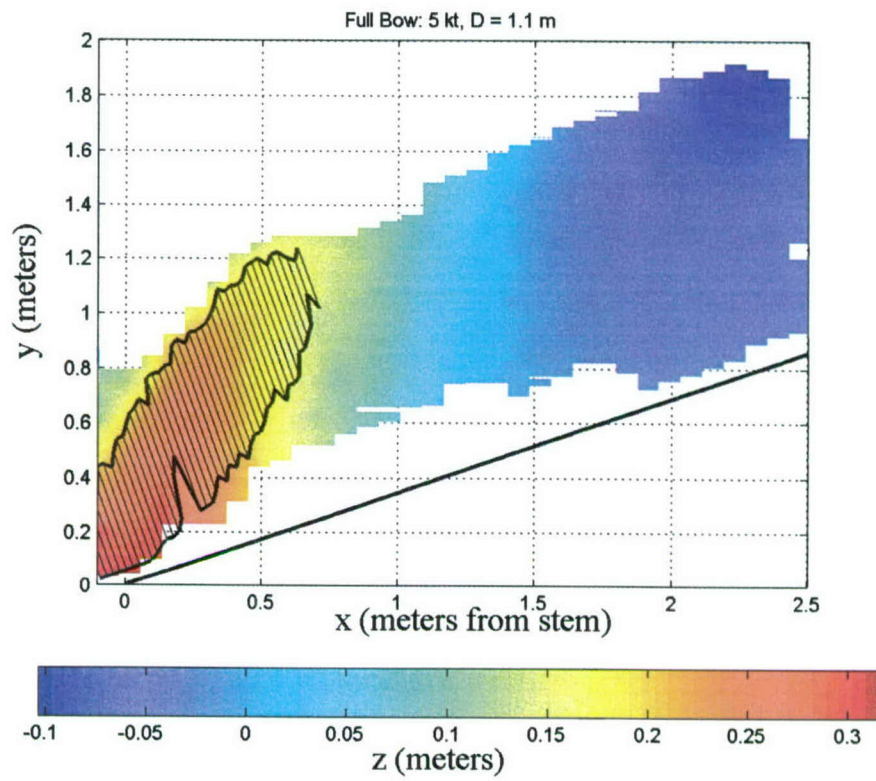
Figure 21. Contour plot of free-surface height with the location of breaking superimposed in black. This run is for the full bow, and has D = 1.1 m, U = 2.6 m/s (5 kt) and Fr = 0.8.
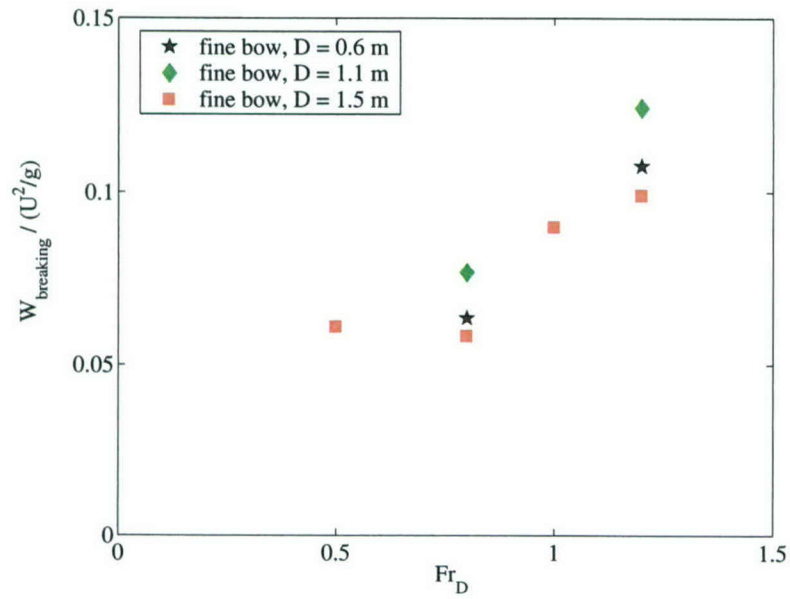
Figure 22. Width of the breaking region for the fine bow, normalized by U^2/g, as a function of draft Froude number.

Figure 23. Width of the breaking region for the fine and full bow, normalized by U^2/g, as a function of draft Froude number.

of draft Froude number. Figure 23 includes the values for the full bow on the same plot, with a new scale. The breaking width has been normalized by the characteristic length for the wave, U^2/g. This normalization relates the width of breaking to the wavelength, $(2\pi)U^2/g$. Figure 22 illustrates that the extent of breaking does increase with increasing Froude number, even when normalized, indicating that the fraction of the wavelength that exhibits rough breaking on the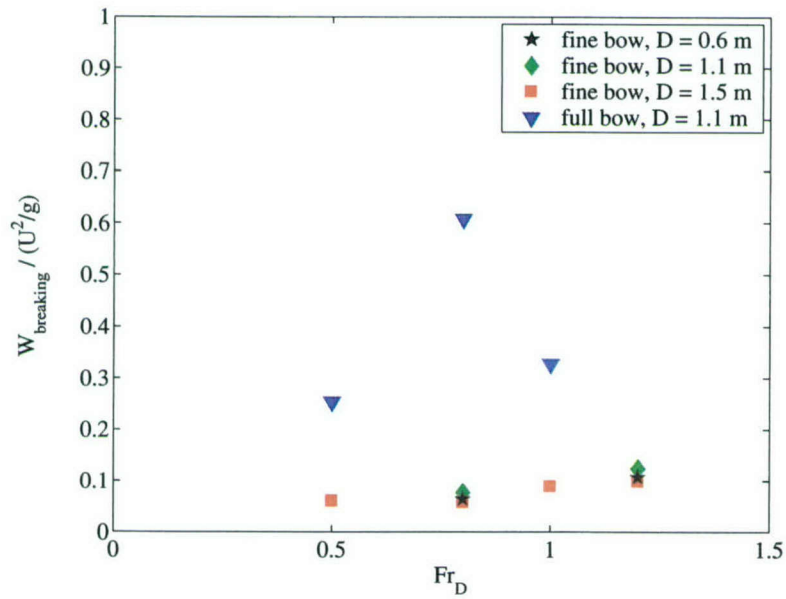 surface is not constant. Figure 23 shows that the hull shape makes a very significant difference, as the width of the breaking region is much larger for the full bow than for the fine bow. The extent of breaking for the full bow seems to decrease from $Fr = 0.8$ to $Fr = 1.0$. This may be at least partially due to a transition in the form of the wave between these two conditions. The bow wave transitions from a spilling breaker that breaks violently ahead of the stem (for $Fr = 0.8$) to a plunging breaker that begins breaking behind the stem, once the bow sheet impinges on the free surface (for $Fr = 1.0$).

High-speed imaging of spray droplets

This section presents some preliminary results from the high-speed video of the bow spray created by the full bow. Only a small fraction of the high-speed video footage from this experiment has been processed to date; therefore, the purpose of this section is: (1) to show what types of measurements are possible with the high-speed video system and (2) to give a rough characterization of the spray generation process and the resulting droplet populations.

Figure 24 presents a typical raw image sequence from the high-speed video camera of the bow spray droplets. The high-speed video camera was positioned at Location 2 (see Figure 1) and was focused on a portion of the crest of the bow wave generated by the full bow at $Fr = 1.1$, $Re = 5.0 \times 10^6$, and $We = 2800$. The camera was focused at approximately $x = 1.3$ m, $y = 1.0$ m, and $z = 0.47$ m with a 21.7 cm (H) by 20.4 cm (V) field of view. The coordinates x and y are defined as in the contour plots in the previous section. The coordinate z is the distance above the undisturbed free surface. The look-down angle of the camera was 25°24'. Not only do these images clearly show the bow-spray droplets, but they also show the details of the spray generation process which will be discussed in the following section.

Figure 25 presents the number of spray droplets counted in each of the 2,176 images as a function of time for the full bow at $Fr = 1.0$, $Re = 3.3 \times 10^6$, and $We = 1800$. Even though the bow wave is a steady breaking wave, local spray droplet populations can be extremely unsteady. For these flow conditions, the number of spray droplets fluctuated about a mean value of 19 droplets per image. Almost all of the runs in these experiments were done in calm water conditions, i.e., a sufficient length of time passed between the runs for the waves in the towing tank to dissipate. However, a few runs were done in rough water conditions where the model was towed forward down the tank, then towed in reverse to the starting position at the maximum "safe" speed, and then towed forward down the tank again with no time delay. The ambient waves encountered by the bow wedge model in these runs increased bow spray production significantly. Figure 26 presents the number of spray droplets counted as a function
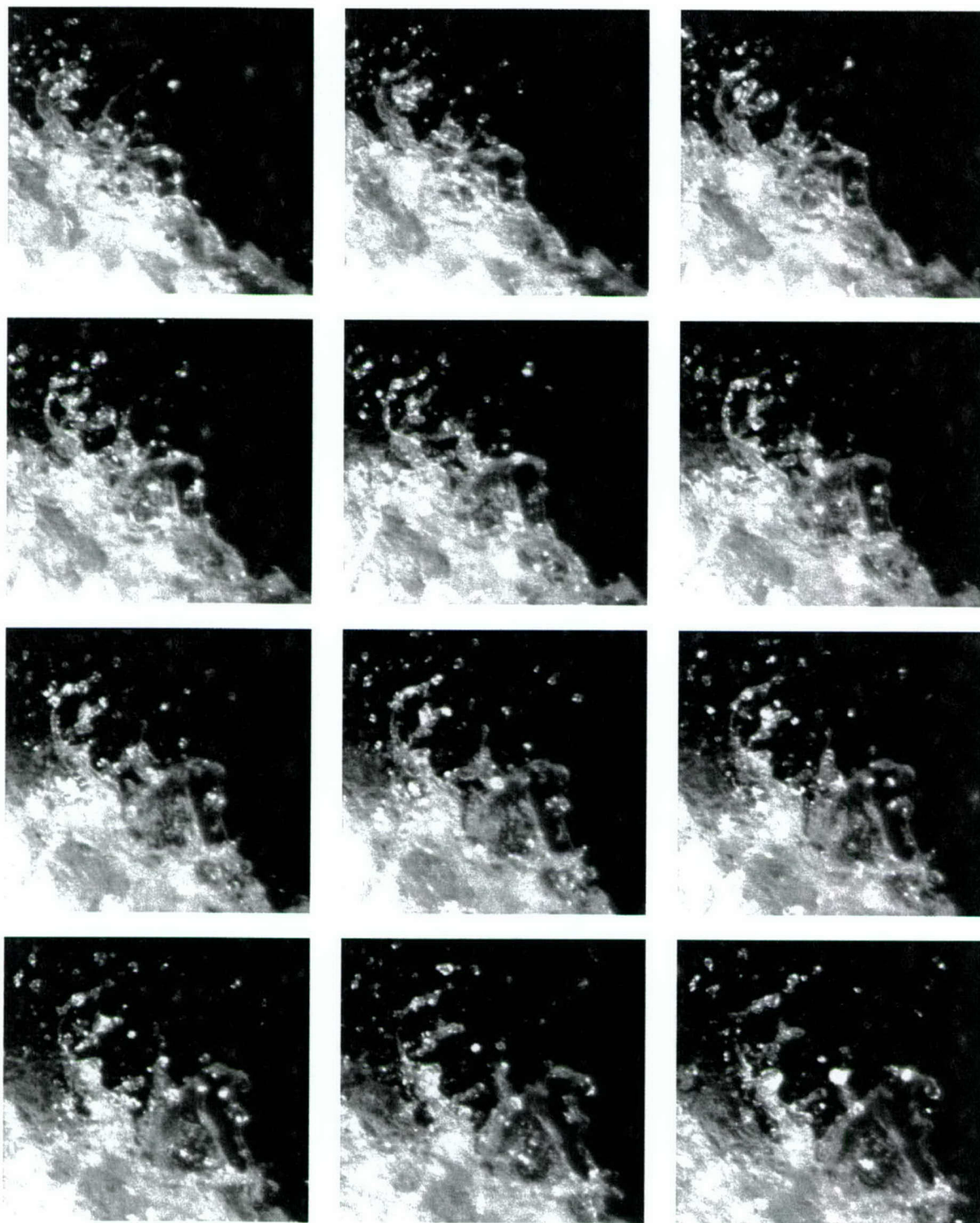
Figure 24. Part of a typical image sequence (12 frames out of 2,176) of spray droplets generated by the full-bow bow wave at $Fr = 1.1$, $Re = 5.0 \times 10^6$, and $We = 2800$. The time between images was 4 ms and the sequence reads from left to right and from top to bottom. The field of view was 21.7 cm (H) by 20.4 cm (V).

27

of time for one of these runs; the number of spray droplets fluctuated about a mean value of 29 droplets per image. The Froude, Reynolds, and Weber numbers and camera location and settings were the same as for the run presented in Figure 26.

Figure 27 shows the numerical frequency (probability density function) of the apparent spray droplet radius for the full-bow bow wave at $Fr = 1.1$, $Re = 5.0 \times 10^6$ and $We = 2800$. The number of droplets is normalized such that the area under the curve connecting the data points is equal to one. The camera's field of view was slightly different than the run presented in Figure 24; it was focused at $x = 0.92$ m, $y = 0.62$ m and $z = 0.49$ m with a 19.9 cm (H) by 18.6 cm (V) field of view. The look-down angle of the camera was 22°36'. The apparent droplet radius, r, was calculated according to $r = \sqrt{area/\pi}$ where the area was the area of the droplet object identified by the image processing program. A total of 102,315 droplets were counted. The bin size for these distributions was 0.05 cm; for example, the fraction of spray droplets with an apparent radius between 1.00 and 1.05 cm is represented by the filled circle at 1.025 cm on the abscissa. The first bin was between 0 and 0.5 mm and did not contain any droplets since it was below the resolution of the high-speed video measurements; it was not included in Figure 27. The mean value of this distribution is 0.23 cm. Based on spray droplet distributions reported in the literature (see, for example, Sarpkaya and Merrill (2001) and Sallam *et al.* (1999)), a more Gaussian-shaped distribution was expected. The shape of these size distributions indicate that there may be a number of smaller droplets that were not captured. A high-speed camera with a higher resolution would be required to capture these smaller droplets.

It is possible to estimate number density distributions from the probability density functions, and an example is shown in Figure 28. This figure should be interpreted with extreme caution because although the field of view is well known, the depth of field is not. At these large working distances (3.9 m) the depth of field is also large and measuring the limits of the depth of field is a somewhat subjective process. For this figure, the depth of field was estimated to be 1 m.

Figure 29 shows the number frequency (probability density function) of the spray droplet velocity for the full-bow bow wave at $Fr = 1.1$, $Re = 5.0 \times 10^6$, and $We = 2800$ for the same run as is presented in Figure 27. It is extremely important to note that the velocities reported here were measured in the focal plane of the camera. Although the spray droplets also move in and out of the focal plane, this movement could not be measured with the existing high-speed video system. The distribution appears to be Gaussian with a mean value of 0.41 m/s and standard deviation of 0.16 m/s. The droplet velocity can also be plotted as a function of droplet size as in Figure 30.

Discussion

The present experiments were run at various Froude and Reynolds numbers; the results are useful for identifying a parameter space for breaking and spray generation. In addition, the Weber number is important to spray generation.
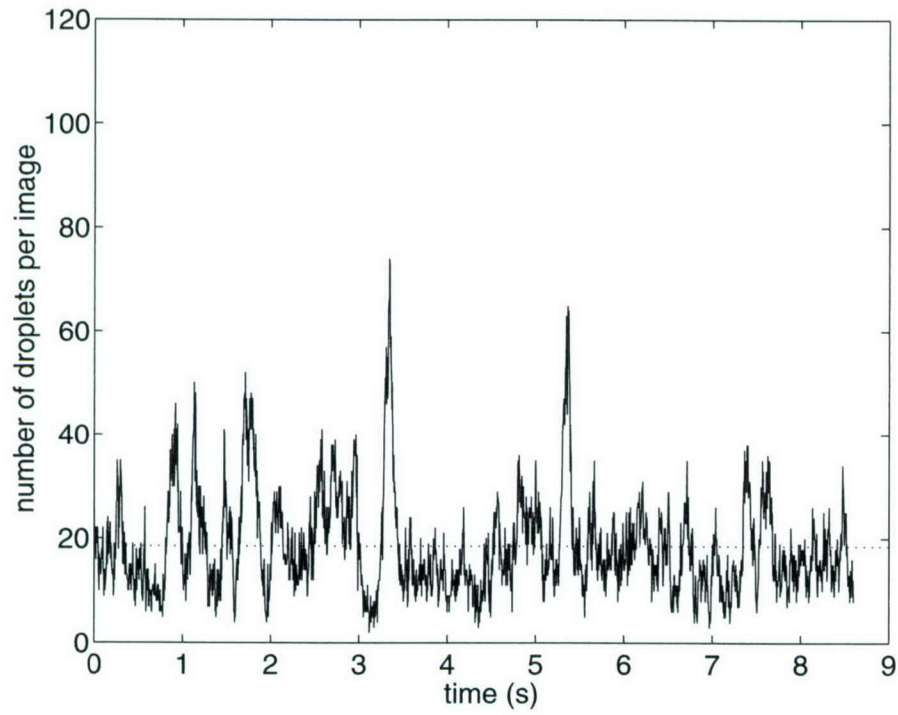
Figure 25. Bow spray generation for full bow in calm water conditions at $Fr = 1.0$, $Re = 3.3 \times 10^6$ and $We = 1800$. The horizontal, dotted line indicates the mean value of 19 droplets per image.
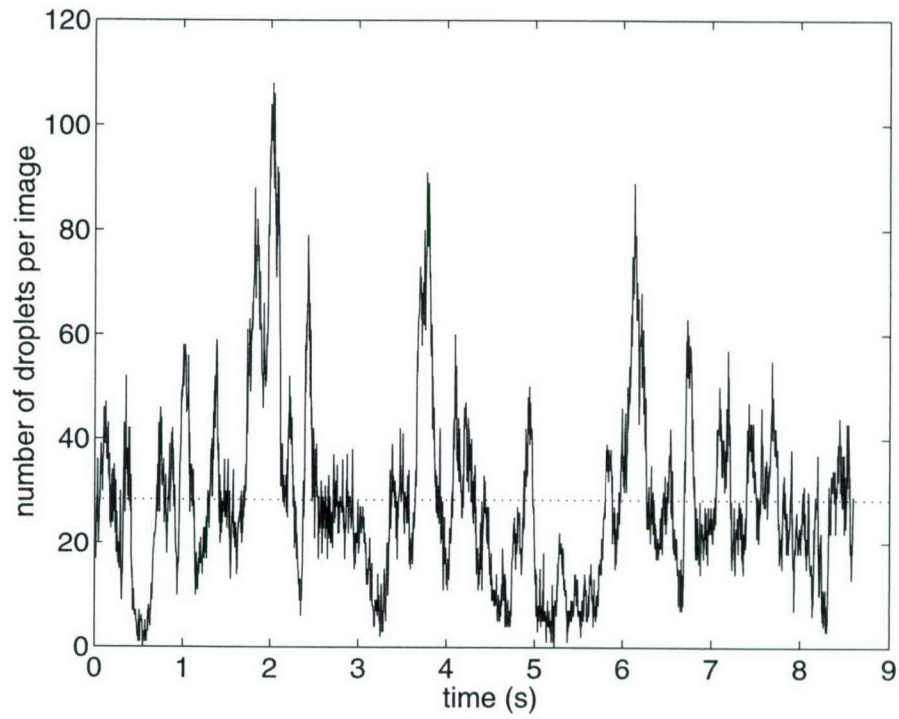
Figure 26. Bow spray generation for full bow in rough water conditions at $Fr = 1.0$, $Re = 3.3 \times 10^6$ and $We = 1800$. The horizontal, dotted line indicates the mean value of 29 droplets per image.
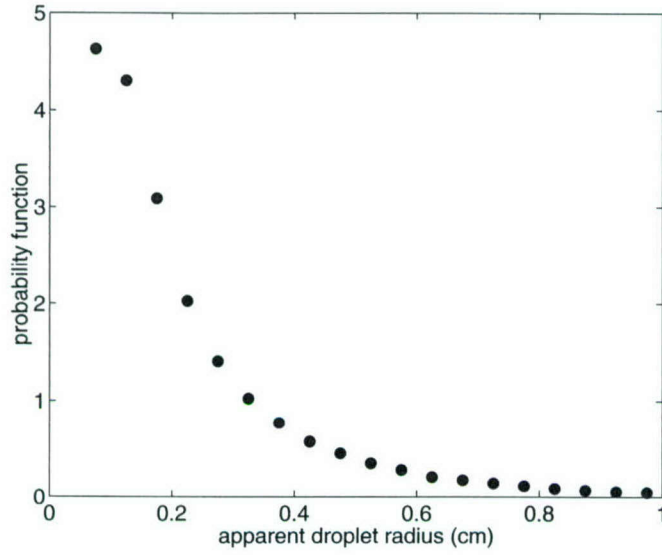
Figure 27. A typical bow spray numerical frequency distribution of the apparent spray droplet radius for the full-bow bow wave at $Fr = 1.1$, $Re = 5.0 \times 10^6$, and $We = 2800$. The mean value of this distribution is 0.23 cm.
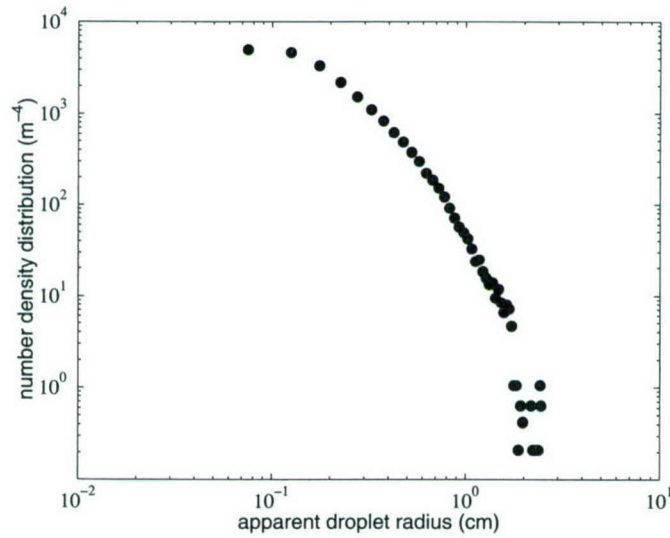
Figure 28. A typical bow spray number density distribution from the results presented in Figure 27, the full-bow bow wave at $Fr = 1.1$, $Re = 5.0 \times 10^6$, and $We = 2800$.
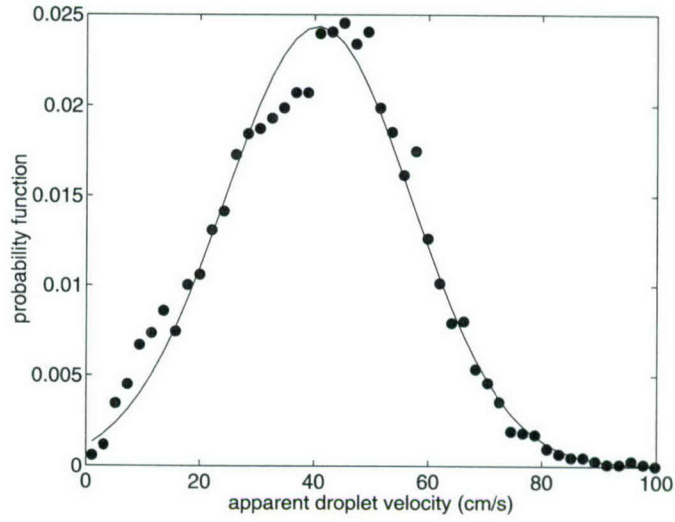
Figure 29. A typical bow spray number frequency distribution of the spray droplet velocity for the full-bow bow wave at $Fr = 1.1$, $Re = 5.0 \times 10^6$, and $We = 2800$ for the same run as is presented in Figure 27. The mean value of this distribution is 0.41 m/s and the standard deviation is 0.16 m/s; the data points are represented by the filled circles and a Gaussian distribution with the same mean and standard deviation is shown by the solid line.
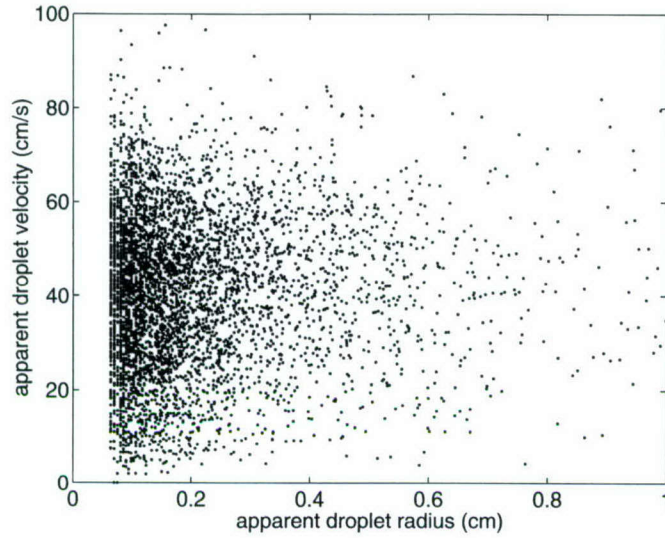
Figure 30. A typical bow spray droplet size-velocity map for the full-bow bow wave at $Fr = 1.1$, $Re = 5.0 \times 10^6$, and $We = 2800$ for the same run as is presented in Figure 27 and Figure 29.

Figure 31 shows the various conditions run during this experiment, along with whether the bow wave was breaking at each. These observations were made by viewing extensive video taken during experimental runs. Breaking was defined as occurring if the sheet of water riding up on the hull curled over and impinged back on the free surface. Figure 32 shows a similar parameter space, illustrating whether spray droplets were observed during the run. There are three cases that show breaking but no droplet generation: on the fine side, $Fr = 0.5$, $Re = 3.0 \times 10^6$ and $Fr = 0.8$, $Re = 1.2 \times 10^6$; and on the full side, $Fr = 0.8$, $Re = 1.8 \times 10^6$. These three cases can be classified as smooth breaking cases, in which the bow wave exhibited curl-over and breaking but did not generate rough white-water conditions. Thus, spray droplets were not observed in the high-speed video of these runs. Figures 31 and 32 illustrate that breaking occurs when both the Froude and Reynolds numbers are high, and transitions to rough breaking (and therefore spray generation) at even greater values of both the Froude and Reynolds numbers.

Figure 33 presents an additional parameter space for spray generation which includes the Weber number, We, the ratio of inertial to surface tension forces. The length scale used in these Weber numbers was the bow radius. The thickness of the thin liquid sheet along the bow wedge model would be more appropriate; however, this quantity was not measured in these experiments. Similar to Figures 31 and 32, Figure 33 shows that the Froude and Weber numbers must both exceed critical values for spray droplets to form.

The various Froude and Reynolds numbers run during this experiment also provided useful data for performing a scaling analysis. QViz data was used to investigate the

Figure 31. Breaking $Fr - Re$ parameter space. The filled symbols indicate flow conditions for which bow wave breaking was observed and the open symbols indicate flow conditions for which breaking was not observed. Triangles represent the full bow of the wedge and circles represent the fine bow of the wedge.
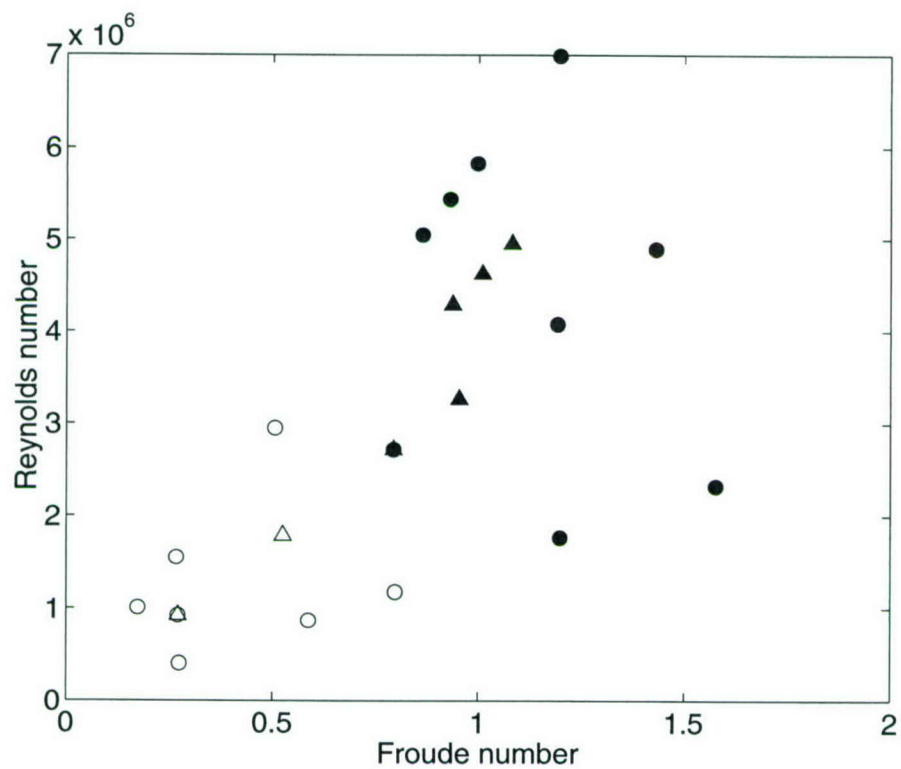
Figure 32. Bow spray $Fr - Re$ parameter space. The filled symbols indicate flow conditions for which spray was observed and the open symbols indicate flow conditions for which spray was not observed. Triangles represent the full side of the wedge and circles represent the fine side of the wedge.
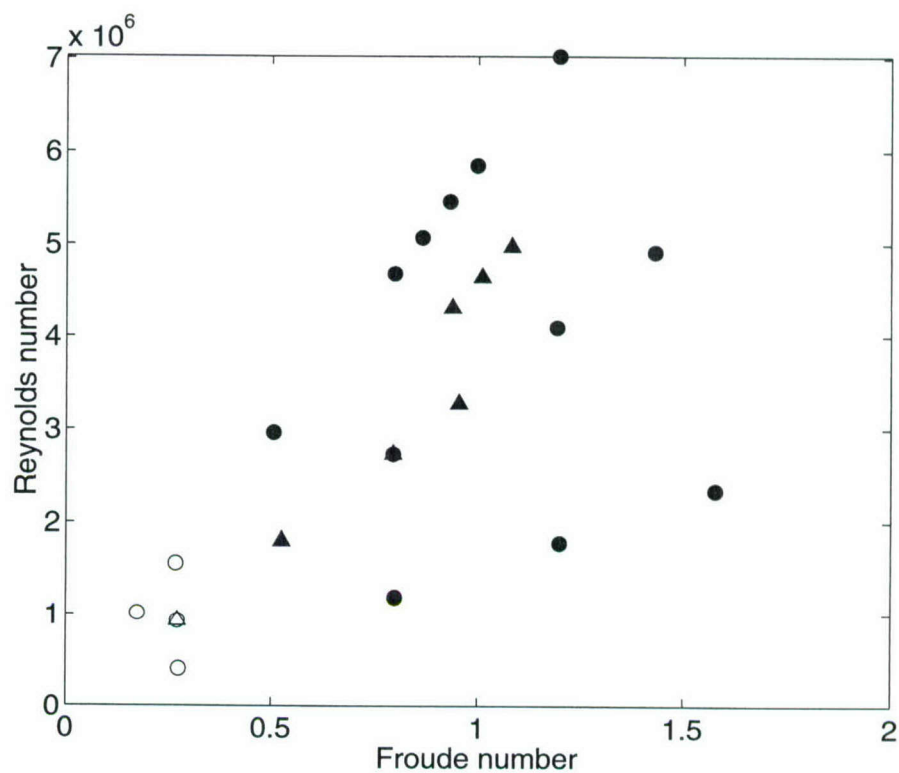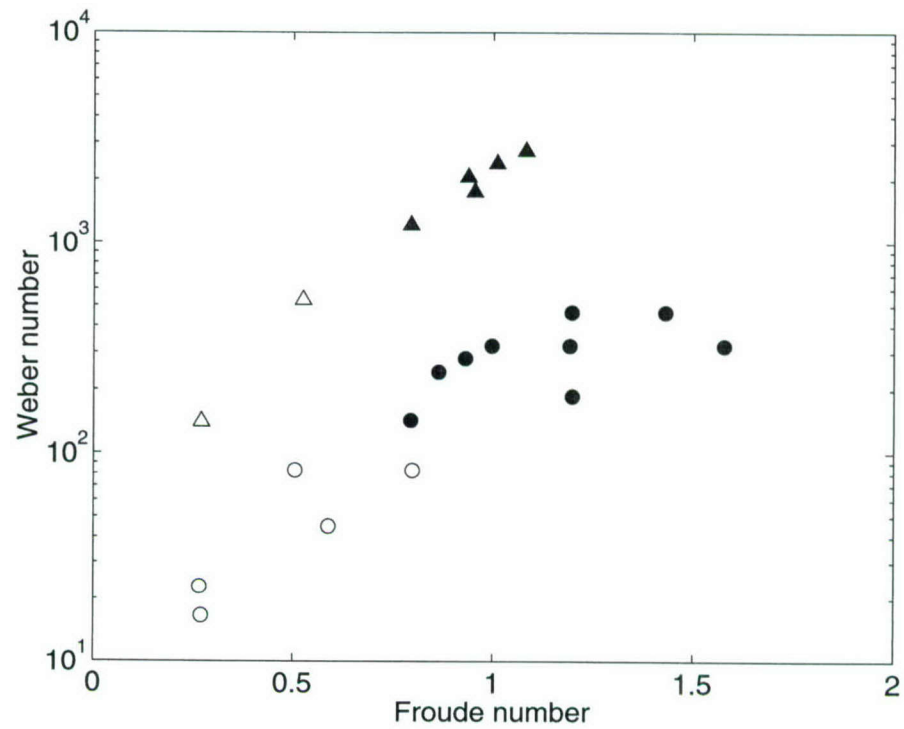
Figure 33. Bow spray $Fr - We$ parameter space. The filled symbols indicate flow conditions for which spray was observed and the open symbols indicate flow conditions for which spray was not observed. Triangles represent the full side of the wedge and circles represent the fine side of the wedge.
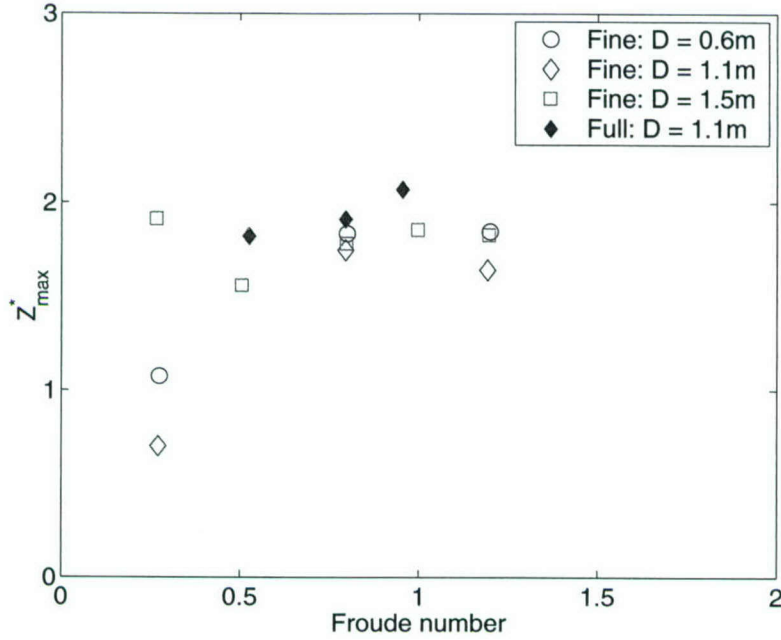
Figure 34. Z_{max}^*, as defined in Equation 4. This is the scaling that Waniewski *et al.* (2002) suggest.

effect of velocity and draft on the maximum wave height, which was extracted from the free-surface contours shown in the previous section. This maximum wave height, Z_{max}, was found to be a strong function of the model forward velocity, U, and a weaker function of the model draft, D.

Waniewski *et al.* (2002) performed experiments similar to those described here, but at a smaller scale. They suggest a scaling of their wave height data as follows:

$$Z_{max}^* = \frac{Z_{max}}{Fr^{1.5}D(2\theta/\pi)},$$

(4)

where Z_{max}^* is a non-dimensional maximum wave height, Z_{max} is the measured maximum wave height, and θ is the bow half-angle. This non-dimensionalization is similar to that suggested by Ogilvie (1972):

$$Z_{max}' = \frac{Z_{max}}{FrD(2\theta/\pi)}.$$

(5)

Ogilvie suggests that for all drafts and speeds (within the valid range of his analysis), the value of Z_{max}' should be constant at approximately 1.6.

In Figures 34 and 35 the maximum wave height data from the present experiment have been non-dimensionalized and plotted using each of these methods. It should be noted here that the three data points at the lowest Froude number of 0.3 have a large

37

Figure 35. Z'_{max}, as defined in Equation 5. This is the scaling that Ogilvie (1972) suggests.

percentage of error. The maximum wave height, Z_{max}, for $D = 1.52$ m is only 4 cm, and the other two have Z_{max} below 1.5 cm. Because the error of the QViz method for this experiment has been estimated to be approximately ± 1 cm, these data points have errors approaching 100 percent! They should be viewed with suspicion; they are simply included here for completeness.
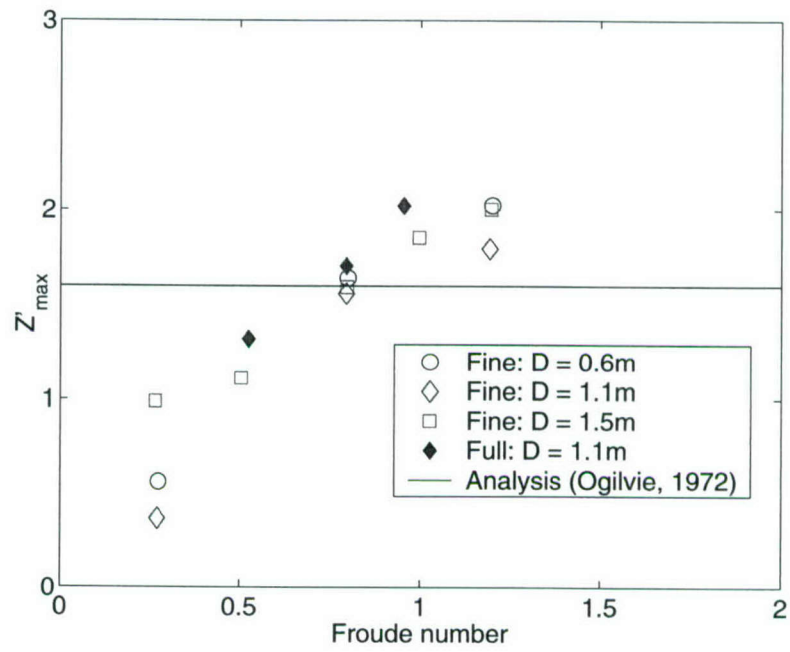
Figures 34 and 35 illustrate that Equation 4 non-dimensionalizes the wave heights from the current experiment better than Equation 5. That is, the wave heights scale better with $Fr^{1.5}$ than with Fr, suggesting a greater dependence on the velocity and a smaller dependence on the draft than that in Ogilvie's (1972) analysis. The results at the two different entrance angles also illustrate that scaling the maximum wave height by the entrance half-angle θ works well, despite the difference in flare angle. This result seems to support the conclusion of Waniewski $et\ al.$ (2002), that the flare only weakly affects the bow wave height. However, the full bow in the current experiments also featured a more rounded leading edge than that of the fine bow. It seems that, at least for the current configuration, the increased wave heights for the full bow can be accounted for simply by assuming a linear dependence on entrance angle.

Figure 36 shows the same data but this time also includes data from Ogilvie (1972) at a 15 degree entrance angle and from Waniewski $et\ al.$ (2002) for both stationary flume and towed wedge experiments at various entrance angles. The current data set fits in well with these two sets. Figure 37 shows the data from the current experiments along with the data from Ogilvie (1972) and Waniewski $et\ al.$ (2002) against the Reynolds number. This figure illustrates that although the Reynolds numbers of the current wedge experiments are significantly higher than those of the previous experiments, the scaling suggested in Equation 4 still holds.

The preliminary results from the high-speed video of the spray droplets presented in the previous section show that a quantitative characterization of the bow spray droplet population is possible for these flows. Further study may lead to the development of empirical relations between quantities such as droplet mean diameter and Reynolds, Froude, and Weber numbers which may help develop and/or validate numerical spray models.

Qualitative observations of bow spray droplet formation are also possible with the standard and high-speed video footage. For example, both the standard and high-speed video show the major regions of spray formation to be: (1) along the crest of the bow wave and (2) along the impact line, where the bow wave impinges on the free surface causing splash-up. Some spray droplets were also thrown forward of the bow wedge model. The high-speed video allowed observation of additional details. By stepping through the high-speed video sequences frame by frame, different spray generation mechanisms could be observed. The three most frequently observed mechanisms were (1) ligament formation and droplet pinch-off, (2) bow sheet thinning and disintegration, and (3) secondary droplet break-up. All types have been reported previously in the literature for similar flows. In the first mechanism, the roughened free surface distorts into ligaments which elongate and thin over time leaving behind strings of droplets. The formation of spray droplets by ligaments has been studied in detail by Sarpkaya
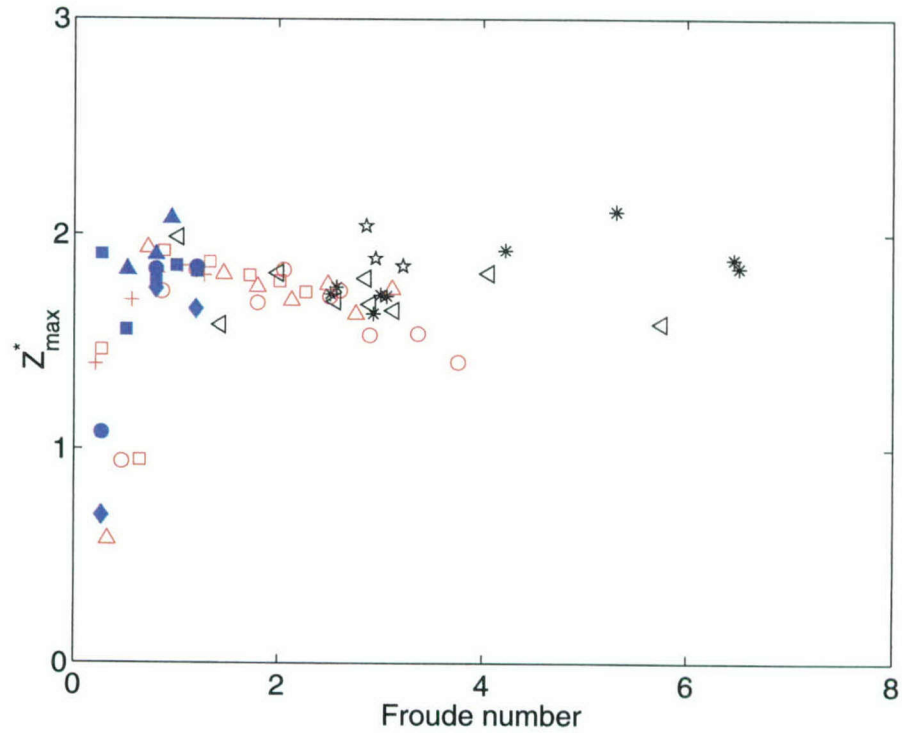
Figure 36. Z^*_{max} from the current experiment, now plotted along with data from Waniewski *et al.* (2002) and Ogilvie (1972). The blue filled circles, diamonds, squares and triangles are from the current wedge experiments. The black open stars, sideways triangles, and asterisks are data from Waniewski *et al.* (2002); the red open symbols and + marks are from Ogilvie (1972).

Figure 37. Z^*_{max} from the current experiment, plotted along with data from Waniewski *et al.* (2002) and Ogilvie (1972), now against the Reynolds number (based on draft). The blue filled circles, diamonds, squares and triangles are from the current wedge experiments; the black open stars, sideways triangles, and asterisks are data from Waniewski *et al.* (2002); the red open symbols and + marks are from Ogilvie (1972).
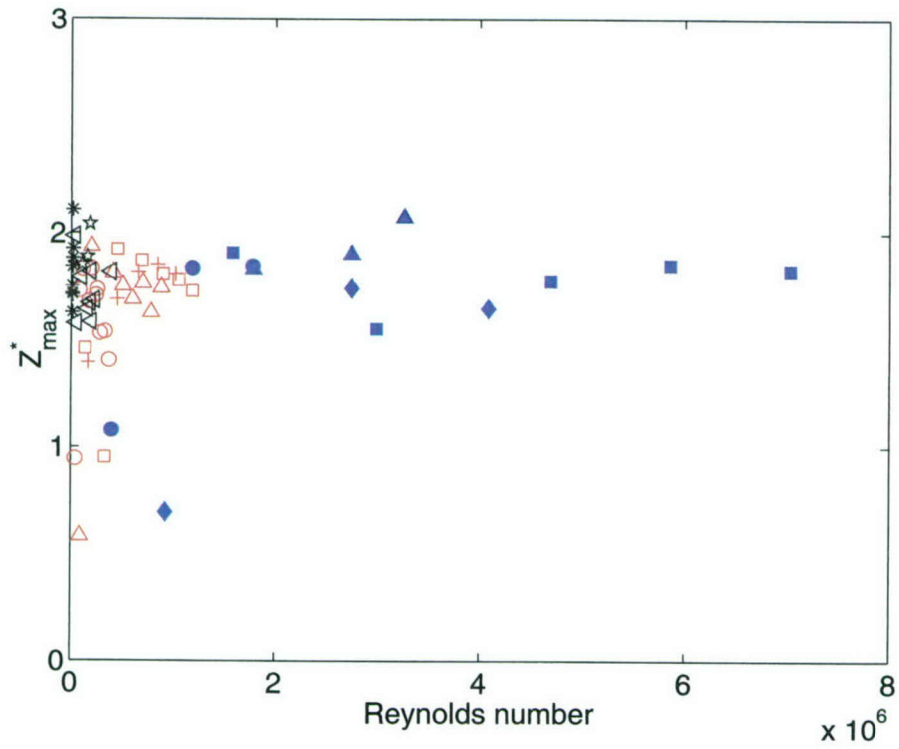
(see, for example, Sarpkaya and Merrill (2000)) for turbulent plane water wall jets under more controlled laboratory conditions. They report the majority of the ligaments giving rise to just one droplet, whereas in these experiments the ligaments appear to thin to the point that a string of droplets is left behind. Bow sheet thinning and disintegration is a more catastrophic type of break-up of the bow sheet seen only at the higher Reynolds, Froude and Weber number conditions. As shown in Figures 25 and 26, the ambient waves significantly increase the spray droplet production especially through bow sheet thinning and disintegration, and this was also observed in the R/V Revelle field experiments. Secondary break-up is when a large droplet separates from the bow sheet and then breaks up again into smaller droplets, and the current image processing algorithms are not sophisticated enough to quantify these events.

Conclusion

Measurements of the bow wave of a large towed wedge in fresh water provide useful data for the validation of numerical modeling techniques. The simple wedge geometry of the model is easier for computational researchers to replicate than that of a real ship bow. The large wave generated can be compared with sophisticated numerical predictions that account for non-linear wave breaking.

Five different results are presented that will aid researchers modeling breaking bow waves. The average height of the free surface in the bow region allows comparison with relatively simple modeling techniques. The magnitude of the free-surface fluctuations is also presented, serving as a measure related to the turbulent energy of breaking. The surface roughness on the face of the breaking wave is presented for cases in which the wave was wide enough to allow a spectrum analysis. The wavenumber information supports previous work in this area, although not enough of the data was able to be analyzed to be conclusive. In addition, the area and location where breaking occurs is shown; the extent of the breaking, normalized by U^2/g, increases with draft Froude number and is significantly larger for the straight-sided (full) bow than the flared (fine) bow. Lastly, spray droplet measurements provide data for comparison with models that account for spray generation. The data and conclusions here can be used to aid in the development of breaking models in the future.

In addition to providing valuable experimental data for validation of numerical models, the present study investigates the effect of scale on bow waves. Measurements were made at a variety of Froude, Reynolds and Weber number conditions, created by varying both the velocity and draft of the model. Observation of the waves at these conditions allows for a determination of the conditions at which bow wave breaking and spray generation occur. Results show that breaking occurs when both the Froude and Reynolds numbers exceed a critical level. At even higher combinations of Froude and Reynolds numbers, the breaking becomes rough, and spray generation is observed. In addition, a critical Weber number must be exceeded for spray generation to occur.

Maximum wave heights measured experimentally have been non-dimensionalized and compared with those of previous experiments by Ogilvie (1972) and Waniewski et al. (2002). Scaling the maximum wave heights by the quantity ($Fr^{1.5}D$), suggested by

Waniewski *et al.* (2002), collapses the data fairly well. Although the Reynolds numbers of the current experiments are significantly higher than those of Ogilvie (1972) and Waniewski *et al.* (2002), the scaling works equally well.

Two different bow shapes were tested in this set of experiments: one bow with a 20 degree entrance angle and a 20 degree flare angle (fine bow), and one with a 40 degree entrance angle and no flare (full bow). In addition, the unflared end's leading edge had a larger radius of curvature than that of the flared end. The full bow generated larger wave heights, and the shape of the bow wave differed from that of the wave generated by the fine bow. For the cases run, the higher crest amplitude can be accounted for by a linear relationship of wave height with entrance half-angle, θ, as first suggested by Ogilvie (1972). More experiments will need to be performed to pinpoint the effect of flare and rounded leading edge.

This page left intentionally blank.

References

Dong, R. R., Katz, J., and Huang, T. T., 1997, "On the structure of bow waves on a ship model," *Journal of Fluid Mechanics*, Vol. 346, pp. 77–115.

Fontaine, E., and Cointe, R., 1997, "A Slender Body Approach to Nonlinear Bow Waves," *Phil. Trans. R. Soc. London A*, Vol. 355, pp. 565–574.

Fu, T. C., Furey, D. A., Karion, A., Mutnik, I., Rice, J., Sur, T. Waniewski, and Walker, D., 2003, "Hydrodynamic Measurements of a Steady Wave During Various Breaking Conditions in the Circulating Water Channel," Carderock Division, Naval Surface Warfare Center, Hydromechanics Research and Development report, NSWCCD-50-TR-2003/12.

Furey, D.A. and Fu, T.C., "Quantitative Visualization (QViz) Hydrodynamic Measurement Technique of Multiphase Unsteady Surfaces," 24th Symposium on Naval Hydrodynamics, 2002.

Iafrati, A. and Campana, E. F., 2003, "A Domain Decomposition Approach to Compute Breaking Waves," *International Journal for Numerical Methods in Fluids*, Vol. 41, 419-445.

Karion, A., Sur, T.W., Fu, T.C., Furey, D.A., Rice, J.R. and Walker, D.C., "Experimental Study of the Bow Wave of a Large Towed Wedge," 8th Int'l Conference on Numerical Ship Hydrodynamics, 2003.

Melville, W.K., Veron, F. and White,, C.J., "The velocity field under breaking waves: coherent structures and turbulence," Journal of Fluid Mechanics, Vol. 454, 2002, pp. 203–233.

Miyata, H. and Inui, T., "Non-linear ship waves," Advances in Applied Mechanics, Vol. 24, No. 1, 1984, pp. 215–288.

Noblesse, F., Hendrix, D., and Kahn, L., 1991, "Nonlinear local analysis of steady flow about a ship," *Journal of Ship Research*, Vol. 35, No. 4, pp. 288–294.

Ogilvie, T. F., "The Wave Generated by a Fine Ship Bow," 9th Symposium on Naval Hydrodynamics, 1972, pp. 1483–1524.

Roth, G.I., Mascenik, D.T. and Katz, J., "Measurements of the flow structure and turbulence within a ship bow wave," Physics of Fluids, Vol. 11, No. 11, 1999, pp. 3512–3523.

Sussman, M. and Dommermuth, D. G., "The numerical simulation of ship waves using cartesian-grid methods," 23rd Symposium on Naval Ship Hydrodynamics, 2002, pp. 762–779.

Walker, D.T., Lyzenga, D.R., Ericson, E.A. and Lund, D.E., "Radar backscatter and surface roughness measurements for stationary breaking waves," Proc. R. Soc. Lond. A, Vol. 452, 1996, pp. 1953–1984.

Waniewski, T.A., Brennen, C.E. and Raichlen, F., "Bow Wave Dynamics," Journal of Ship Research, Vol. 46, No. 1, 2002, pp. 1–15.

Wyatt, D.C., "Development and Assessment of a Nonlinear Wave Prediction Methodology for Surface Vessels," Journal of Ship Research, Vol. 44, No. 2, 2000, pp. 96–107.

Distribution

Copies

NAVSEA
| 1 | 05T | A. Reed |
| 1 | | DTIC |

ONR
| 1 | 333 | P. Purtell |

DIVISION DISTRIBUTION
1	3442	TIC
1	5060	D. Walden
1	5300	D. Furey
1	5200	D. Walker
1	5200	D. Hendrix
1	5200	T. Ratcliffe
1	5600	T. Fu
1	5600	J. Rice
1	5600	A. Karion
1	7410	A. Smith (electronic copy only)
1	7406	S. Russell
1	632	file (CD only)

SAIC
| 3 | | T. Sur, D. Wyatt, D. Dommermuth |

Stevens Institute of Technology
| 1 | | L. Imas |